A novel approach to actuate soft robotic catheter via magnetic actuation method.

Chengdong Xu

Master's by Research

University of York

Physics, Engineering and Technology

July 2024

Abstract

We addressed the challenges of navigating within the human chest using a soft magnetic catheter by enhancing the robot workspace and reducing the required magnetic field strength. By increasing the concentration of NdFeB nanoparticles, we successfully decreased the necessary magnetic field. Our proposed methods include utilizing a suitable magnet to achieve actuation inside the body, such as within the bronchi. Our design and simulation studies aimed at improving the robot's workspace and lowering the magnetic field strength needed for actuation. We achieved significant advancements, with the capability to generate the required magnetic field strength at 80% of the locations inside an average-sized body. We demonstrated successful navigation within transparent bronchi over an actuation distance of 110mm. This work highlights the potential for improved internal body navigation using our enhanced magnetic catheter system.

Declaration

I declare that this thesis is a presentation of original work and I am the sole author. This work has not previously been presented for an award at this, or any other, University. All sources are acknowledged as References.

Commitment to non-plagiarism

I, Chengdong Xu, master's student in the School of Physics, Engineering and Technology at the University of York certify that I read the content of the School's Internal Regulations and the "non-plagiarism" commitment. I declare that I comply with it in the drafting of this document. I declare on my honour that the content of this dissertation is original and reflects my personal work. I certify that quotations are correctly indicated by quotation marks and that the sources of all occasional borrowings from other authors, textual or non-textual, are indicated. Failure to comply with this commitment would expose me to sanctions of which I am aware.

Name: Chengdong Xu

Signature: *Chengdong Xu*

Date: 10 July 2024

Acknowledgements

This study towards exploring and overcoming the distance limitations inherent in magnetic robotic surgery has been both challenging and enriching. It is a path I could not have traversed without the support, guidance, and contributions of many individuals and entities whose assistance has been invaluable. First and foremost, I extend my deepest gratitude to my supervisors, Dr Manish Chuhan and Dr Samadhan Patil, whose insights, expertise, and unwavering support have been the cornerstone of this research. Their guidance has not only shaped this work but has also contributed significantly to my personal and professional growth.

I would also like to express my sincere appreciation to Jack Clarke and Quentin Coulombeaux, whose technical expertise and dedication were crucial in setting up the experiments that enabled us to analyse the bending angle of the catheter. Jack's meticulous approach to problem-solving and his commitment to excellence have been instrumental in the success of our experimental trials.

The journey of completing this thesis has been a testament to the power of collaboration and the importance of community within research. To all those who have offered their time, resources, and wisdom, I am eternally grateful. Your contributions have not only facilitated this research but have also enriched my experience and understanding of the field.

Lastly, I extend my gratitude to the entire department and all my peers for creating an environment of encouragement and intellectual curiosity. This thesis stands as a product of not just my efforts, but the collective support and guidance of everyone who has been a part of this journey.

Table of Contents

Introduction

Minimally invasive surgery (MIS) employs image-guided techniques to diagnose and treat various diseases across almost all organ systems. Over the past twenty years, MIS has significantly transformed surgical practices. This approach reduces physical trauma for patients, leading to lower infection rates, faster recovery times, and shorter hospital stays[1]. Magnetic actuation significantly enhances minimally invasive surgery (MIS) by enabling precise control and flexibility in surgical instrument manipulation, facilitating smaller incision sizes due to compact instrument design, and improving surgeon ergonomics for reduced fatigue during procedures[2]. It also introduces remote control capabilities essential for telesurgery and robotic-assisted surgeries, thereby increasing access to surgical care. The non-contact nature of magnetic systems reduces infection risks, while their compatibility with imaging technologies like X-rays and Computed Tomography (CT) enhances real-time surgical precision. Furthermore, magnetic actuation encourages the development of innovative surgical techniques and is adaptable across various procedures, ensuring safety and reliability in the sensitive environment of the human body. This technology stands as a pivotal advancement in MIS, promising better surgical outcomes, and patient recovery experiences. However, actuating the magnetic soft catheter outside of the human body with one magnet is still challenging especially inside of the chest. This research aims to identify and evaluate the new method of design of magnet and magnetic catheter as well as navigation at the bronchi model in the average size of the human chest.

A wide array of studies has explored the application of magnetic materials in catheter design, magnetic actuation and demonstrating various degrees of success in improving maneuverability and reducing procedural risks[3-14]. These studies collectively underscore the potential of integrating soft robotics into catheter technology to overcome traditional limitations. The design of the catheter can be either continuous or discrete. Lalande et al. [15] showcased the in vivo steerability of a magnetic guidewire using an MRI system. The guidewire featured a ferromagnetic bead affixed to its tip. The MRI system's coils created a magnetic gradient that exerted a force on the bead, enabling the guidewire to be directed as needed. Experiments with two rabbits demonstrated the guidewire's navigation and steering capabilities. While the renal arteries showed higher success rates, attempts in other areas were mostly unsuccessful. The primary challenge was the lack of real-time navigation due to hardware limitations, which prevented simultaneous steering and tracking. The steering gradient coils in the MRI system rendered imaging impossible, forcing control of the guidewire to rely on previous tracking data.

In 2017, Edelmann et al[3]. developed a flexible guidewire-based microrobot for small animals. Jeon et al. [4] improved this in 2018 with a magnetically controlled system enhancing guidewire steerability for coronary use. By 2019, Kim et al. [16] had created a ferromagnetic soft robot for cerebrovascular interventions, capable of navigating complex vascular networks. Additionally, they introduced a teleoperated neurointerventional platform. In 2020, Pittiglio et al. [6] advanced this technology with a dual-arm system for more precise magnetic manipulation.
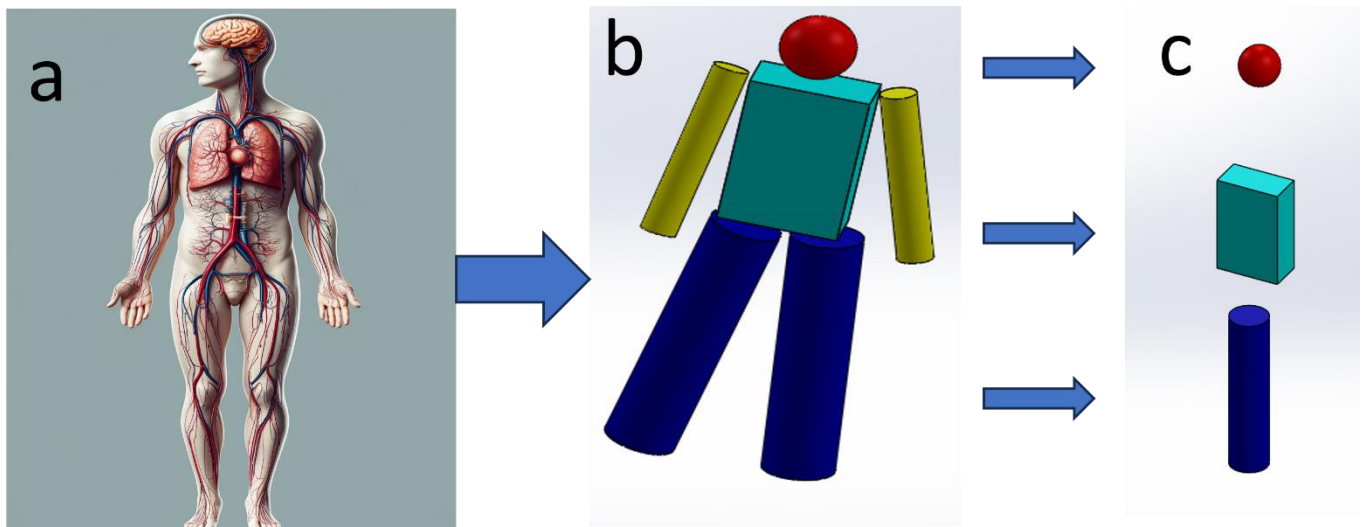
Figure 1Conceptual breakdown of a human body into simplified geometric shapes：(a) Depicts a detailed anatomical representation of a human body, showing the internal structure such as the brain, heart, and blood vessels. （generated by GPT-4） (b) Represents the human body using simplified geometric shapes. The head is shown as a red sphere, the torso as a teal cube, the arms as yellow cylinders, and the legs as blue cylinders. This abstraction simplifies the human form into basic components for easier analysis. (c) Further deconstructs the simplified human model into its individual components. The head, torso, and limbs are shown separately as distinct shapes (a red sphere, a teal cube, and blue/yellow cylinders)

The size of the organ, magnetic field needed, direction and strength of the magnetic field can be applied in the target area are crucial for the magnetic actuation in MIS. Numerous studies have managed to address this problem[3, 9, 11-14]. Current research in the field has predominantly been confined to applications targeting specific diseases, leading to an approach that narrows the focus to certain navigation paths and magnetic actuation distances. Specifically, these studies have tailored their methodologies around navigating to specific organs, including the head, neck, limbs, and feet, where the magnetic driving distance is inherently linked to the target organ's location. This specificity, while beneficial for targeted applications, significantly hampers the adaptability of the technology. It renders current systems less capable of addressing complex navigational routes or achieving propulsion over greater distances than those for which they were initially designed. For example, the human body can be simplified into geometric shapes like sphere, cube and cylinders for easier analysis as illustrated in Figure 1, while current research focus on provide magnetic field using axial of cylinder magnet (Figure 2 (a)), which perfectly fine with sphere, using axil area of cylindrical magnets to provide a magnetic field along the long direction of wide or long cubes and long cylinders faces significant challenges as show in Figure 2, as maintaining a strong magnetic field along a long direction requires very strong magnets, which is impractical, as indicated by the magnetic field intensity gradient.
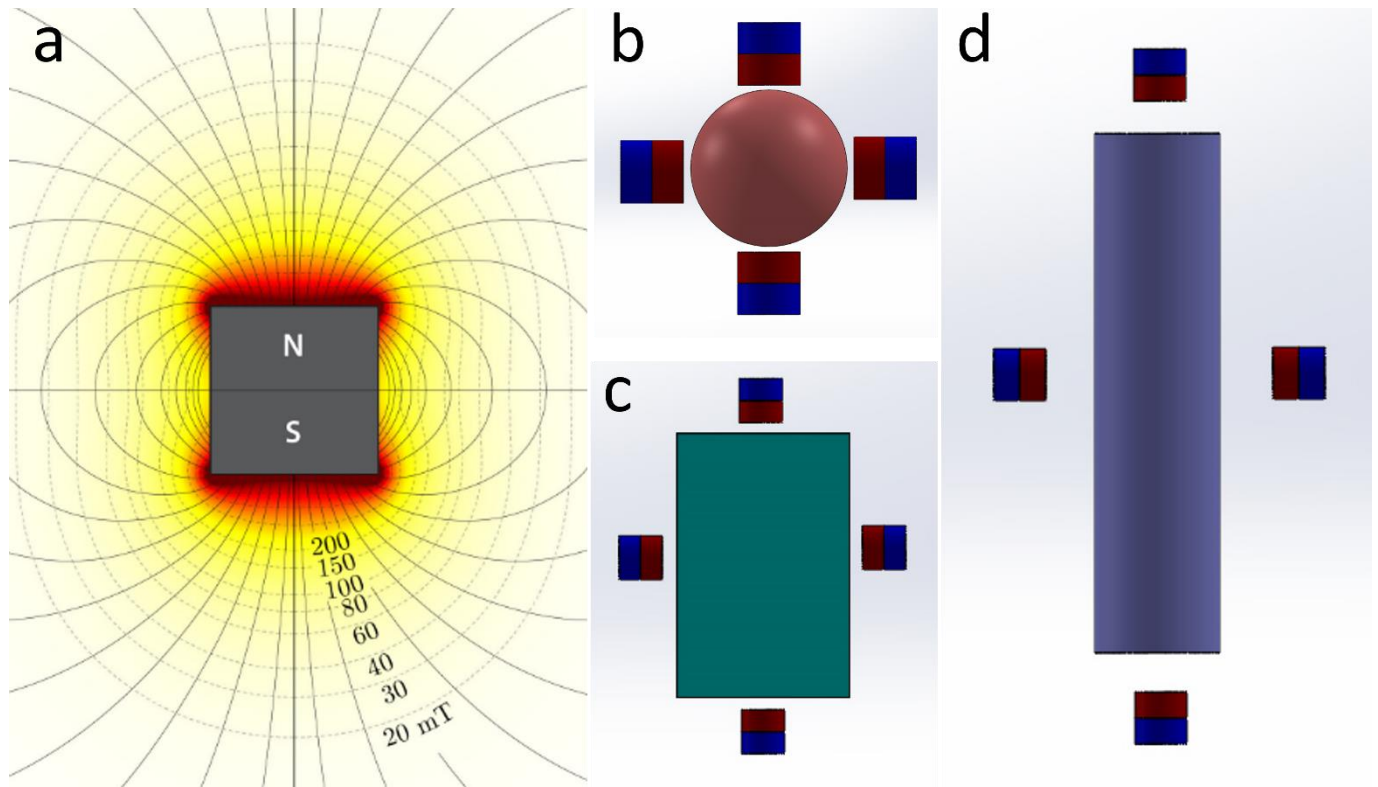
Figure 2 (a) Shows a magnetic field representation around a bar magnet. The field lines emanate from the north (N) pole and loop around to the south (S) pole, illustrating the magnetic field intensity with color gradients. The numbers indicate the magnetic flux density in milliteslas (mT). (b) Shows a sphere (possibly representing the head from the previous image) with four small magnets positioned around it, suggesting a simplified model for a magnetic head configuration. (c) Displays a rectangular prism (which could represent the torso) with the same configuration of magnets at the corners, indicating a similar magnetic field setup for a rectangular model. (d) Illustrates a cylindrical shape (representing a leg) with the magnets placed around it, indicating how the magnetic field configuration can be applied to a cylindrical model.

Such limitations notably restrict the versatility of magnetic-driven microrobots, confining their utility to a narrow scope of clinical applications and preventing their adoption for broader medical interventions that require intricate maneuvering or navigate beyond short, predefined distances. Consequently, there is a pressing need for future research to overcome these barriers. Innovations that enable flexible navigation capabilities and extend the effective range of magnetic actuation within the human body would markedly broaden the applicability and impact of microrobotic systems in MIS.

Given the lack of research regarding magnetic soft catheters in MIS, the objective of this research is to introduce a novel design and actuation methodology that significantly enhances the adaptability of magnetic soft robots within the human body. This approach is aimed at improving the robots' capability to navigate the complexities of internal structures such as blood vessels and bronchial tubes of the lungs without considering specific path toward the target. Furthermore, it is designed to ensure adaptability across various parts of the body, especially in the chest.
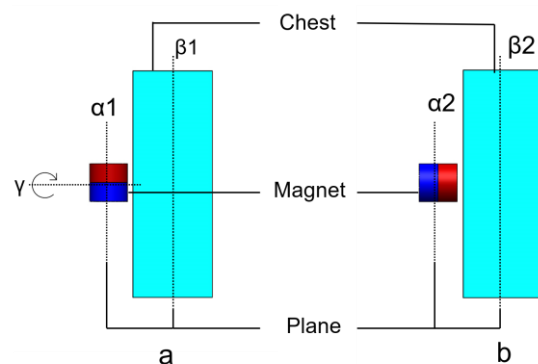
Figure 3 Two primary magnetic drive modes for generating magnetic fields in the chest cavity: (a) cylindrical surface magnet mode with movement along plane α1 or rotation around axis γ to produce a magnetic field on plane β1, and (b) bottom/top surface magnet mode with movement along plane α2 to generate a magnetic field on plane β2.

The innovation of this work lies in the use of the driving method illustrated in the Figure 3, which leverages magnetic fields in various directions around a cylindrical magnet to provide the necessary magnetic field within the chest cavity. This approach contrasts with traditional methods (Figure 2) that rely solely on the axial magnetic field of a cylindrical magnet, which is hard to provide magnetic fields in arbitrary directions when applied to the chest (Figure 2c) or limbs (Figure 2d) as the distance between magnet and target area become too long while the strength of the magnetic field decrease along with distance. In another words, utilizing the magnetic field along the lateral surface of a cylindrical magnet requires a smaller cylindrical magnet compared to using rotation to achieve the same magnetic field.

This research details the design, fabrication, and testing of a magnetically actuated soft robot tailored for navigation within pulmonary bronchi and blood vessels. The robot is a 2 mm diameter, 40 mm long cylindrical structure made from a 1:1 mixture of silicone elastomer and neodymium-iron-boron (NdFeB) particles. This composition ensures strong magnetic properties while maintaining flexibility. The cylinder is magnetized along its axis using a 5T magnetic field to minimize the magnetic field strength required for actuation or bending. Mathematical modeling was used to analyze the effects of magnetic particle content, magnetizing field intensity, and external magnetic field strength on the robot's performance. A novel actuation method employing cylindrical NdFeB magnets was introduced, and COMSOL simulations were conducted to determine the smallest effective magnet size under critical conditions. The fabrication process involved molding the silicone-NdFeB mixture into the desired shape and magnetizing it. An accuracy testing platform was developed to evaluate the precision of the robot's movements under an external magnetic field, providing data to optimize the design and actuation system. In-vitro demonstrations showed the robot successfully navigating to various parts of the pulmonary bronchi using the proposed actuation method, underscoring its potential for medical applications. This research presents a thorough approach to designing, modeling, fabricating, and testing a magnetically actuated soft robot, showcasing high precision and effectiveness in navigating complex internal pathways. This research will contribute to the application of magnetic actuation catheter in MIS with better adaptability by proposed design method of the catheter actuation and future work will focus on refining the design and expanding its clinical applications.

Literature review

The most common type of cancer diagnosed worldwide, and the leading cause of cancer death is lung cancer. Lung cancer has a terrible prognosis, and 75% of patients receive an advanced-stage diagnosis[17]. Excisional biopsy of an accessible node, bronchoscopy, transthoracic needle aspiration, and thoracentesis of pleural effusion are a few procedures that can help doctors acquire an accurate tissue diagnosis[18, 19]. With a combined sensitivity of 88% in patients with central tumors, flexible bronchoscopy (including bronchial washings, brushings, and biopsies) is frequently the test of choice in these patients.

A more recent technique called video-assisted thoracoscopy can be used to sample pleural tumors, pleural effusions, and tiny peripheral tumors (less than 2 cm in diameter) for staging or diagnostic purposes[20]. With the development of soft robotics, there are some robotic platforms to replace former diagnosis tools. However, several issues remain, including force transmission, control, dexterity, and downsizing [21].

I. Minimally invasive surgery

The advent of minimally invasive surgery (MIS) was made possible by Hopkins' creation of the rod-lens endoscope in the 1960s. Then, in the 1970s and 1980s, MIS through a formative phase of clinical assessment and technological advancement before thriving and becoming well-established across the majority of surgical fields [22]. Surgery underwent a revolution when Mouret conducted the first laparoscopic cholecystectomy in 1987. There are three main benefits. First, avoiding big wounds should reduce postoperative pain, which should reduce morbidity brought on by immobility, including postoperative atelectasis and venous thrombosis. Second, preventing a wound should hasten hospital departure and reduce recovery time. Thirdly, improved cosmesis should result from the laparoscopic surgery's tiny portholes [23]. In comparison to MIS techniques, patients receiving open spinal surgery were 5.77 times more likely to improve SSI [24] Population-level data showing shorter and less strenuous hospital stays for kidney cancer patients who underwent laparoszcopic partial nephrectomy corroborate the advantages of laparoscopy [25]. According to the survey by Bostanci et al, which are corroborated by parental assessment, provide the first confirmation that minimally invasive treatment of PC malformation improves the patient's psychosocial and physical functioning [26].

Despite the capability of modern robotic systems to meet the manipulation demands of various surgical applications, the adoption of robot-assisted minimally invasive surgery (MIS) over traditional open surgery or manual laparoscopic surgery has not been universally embraced across all surgical specialties. This low adoption rate is influenced by socioeconomic factors and the difficulty of performing cost-benefit analyses based on post-operative outcomes. However, significant technical challenges also play a crucial role. For the purpose of this discussion, we will focus on the technological difficulties. MIS can be categorized into procedures performed in shallow, wide areas and those in deep surgical fields with limited access and visibility [27].

The utilisation of wire actuation and continuum arms/linkages with substantial deflections and frictional and motion losses is a distinguishing feature of robotic platforms in MIS. These losses make it difficult for these surgical systems' motion control accuracy. Numerous studies have looked at ways to increase the precision of such controls during surgical procedures. The majority of studies used extrinsic measures to close the error online in the control loop [27]. Camera is regard as one of the popular methods as feedback of environment for closed control loop especially in endoscopy. However, most of the endoscopy or robotic platforms are manually controlled which need physicians to be trained for a long time and human would more likely make mistakes when they feel tired which is one of the safety problems during operations. With the development of the artificial intelligence, the automatic endoscopy should be developed to address this issue.

II. Bronchoscopy

In 2020, 1.79 million people died from lung cancer, making it the most frequent type of cancer [28]. These shocking epidemiological findings are primarily due to the lack of appropriate and efficient screening techniques [29]. When the nature and stage of lung cancer are unclear, alternatives such as sputum cytology, flexible bronchoscopy, and transthoracic needle aspiration can be utilized [18]. Flexible bronchoscopy, while relatively non-invasive, has limitations; white light bronchoscopy (WLB) alone is only 29% effective at detecting carcinoma in situ (CIS) and 69% effective at identifying microinvasive tumors. To enhance the diagnostic accuracy and yield of bronchoscopy, various advanced techniques have been developed over the past two decades [20]. These include radial endobronchial ultrasound (R-EBUS), optical coherence

tomography (OCT), confocal laser endomicroscopy (CLE), and laser Raman spectroscopy (LRS), which address the limited specificity and are not restricted to detecting only the proximal bronchial tree [30].

However, It becomes tough during the diagnosis and surgery of lung cancer when facing a fairly small nodule, due to their enormous diameter, which is often greater than 2mm, conventional bronchoscopes cannot easily pass into the peripheral lung and reach small bronchi [31, 32]. In order to visualise lung tumours, they created a unique 2mm-soft catheter with magnetic actuation that can reach bronchi that are larger than 2mm in diameter. Comparatively speaking, magnetic actuation offers superior accuracy and stability, which can increase operating safety[2].

III.   Design of robotics in endoscopy

a) Structural design principles

For soft robotics:

In designing continuum robots, two crucial concepts are stiffness and range of motion (workspace). The robot must have sufficient workspace and stiffness to exert the necessary tissue forces and reach the required areas during its intended process. The backbone's cross-sectional shape and the elastic strain limits of its materials significantly influence these characteristics. Smaller manipulators with higher elastic limits tend to have wider ranges of motion because strain during bending correlates with the distance from the backbone's neutral axis. However, materials with higher elastic strain limits often have a lower elastic modulus (Young's modulus), and reducing the cross-sectional diameter decreases the cross-sectional moment of inertia. This results in a fundamental trade-off between range of motion and output stiffness for continuum robots: improving one typically reduces the other. Therefore, backbone materials with high elastic stress limits (the product of Young's modulus and elastic strain limit) are preferred to achieve both large workspace and high stiffness. This criterion partially explains the widespread use of superelastic NiTi (nickel-titanium) backbone components in continuum robots. Although many steels and carbon fiber composites are less expensive and have relatively high elastic stress limits, they can be machined (e.g., into spiral or patterned tubes) to mimic NiTi's bending properties. NiTi is more frequently used due to its biocompatibility and the availability of thin-walled tubes [33].

For hard robotics:

Generally, hard robotics in MIS refer to capsule endoscope which usually have sensors like camera, batteries for power supply, CPU for signal processing [34]. As for the design of the capsule endoscope, size matters a lot so that everything inside of the capsule must be necessary and well organized. Tognarelli et al[35]. developed an endoscopic robotic capsule featuring a shape memory alloy (SMA)-based anchoring mechanism for internal movement. This capsule is equipped with three active, flexible legs that have strain gauge sensors to measure the stress applied to the tissue. An onboard actuator, controlled by a microcontroller, allows the legs to be deployed and retracted as necessary. The design must take into account both the force exerts on the tissues and the biocompatibility as long as the tissues are affected.

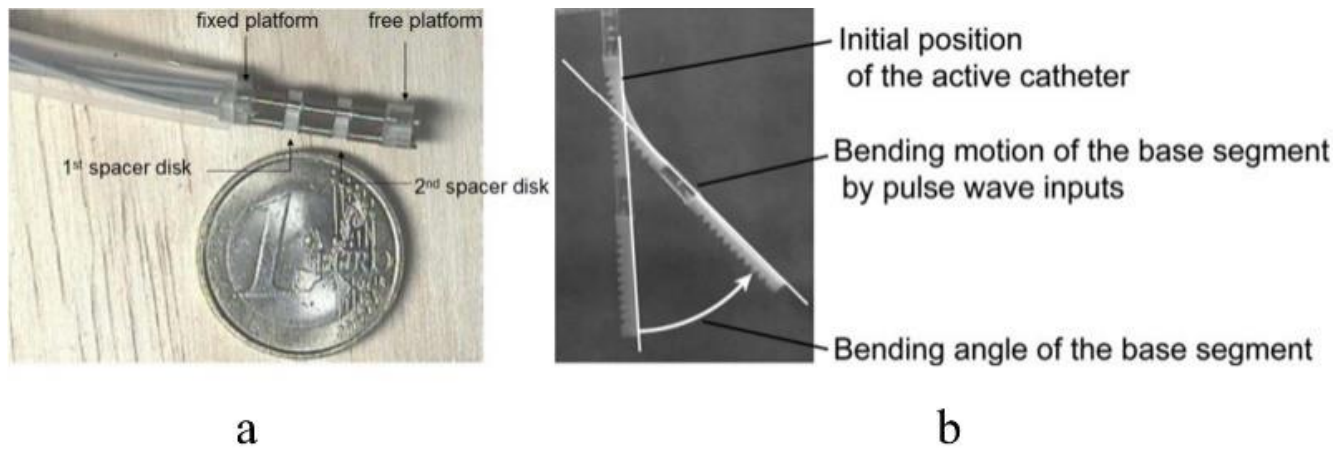## b) Hydraulic Active actuation

Figure 4 Two different hydraulic catheter for MIS [36, 37]

Bailly et al described (Figure 4 (a)) [37] a continuous microrobot in the study that can steer the position of a catheter's distal extremity during endovascular surgery. The microrobot's design incorporates three electrodeposited nickel bellows that connect two cylindrical platforms, providing the necessary properties of compliance and compactness. Its small size allows for easy integration into standard catheters, with dimensions of 4.9 mm in diameter and 20 mm in length. To meet the safety requirements for endovascular surgery, the microrobot is actuated by hydraulic pressure instead of electrical power within the patient's body.

A novel control strategy for the hydraulic active catheter has been put forth in the research of Ikuta et al (2012) [36] as show in Figure 4(b). The active catheter is softer and more compatible with MRI than other catheter-like devices currently under development or in use since it is entirely made of nonelectric and non-metallic components.

c) Conducting polymer actuation:

Nagoya University proposed an active guide wire which has two bending degrees of freedom in 1995 [38]. They prove that the structure of the micro catheter with active wire is effective for traditional intracavity operations.

d) Piezoelectrically actuated tubes:

Su et al. [39, 40] introduced an MRI-guided concentric tube continuum robot with piezoelectric actuation. This 6-DOF robot comprises a modular 3-DOF cannula driver with a fiducial tracking frame and a 3-DOF actuated Cartesian stage. The cannula driver provides 1-DOF translation of the inner stylet and 2-DOF rotation and translation of the precurved middle tube. The compact design includes disposable collect fixtures and a timing belt mechanism for rotational movement. The Cartesian stage controls the outer cannula with 1-DOF along the insertion axis and 2-DOF lateral motion for alignment. Position sensing feedback for closed-loop control is achieved using optical encoders (US Digital, Vancouver, Washington) and piezoelectric actuators (PiezoMotor, Uppsala, Sweden). Figure 5 [40] provides a close-up view of the active cannula robot.
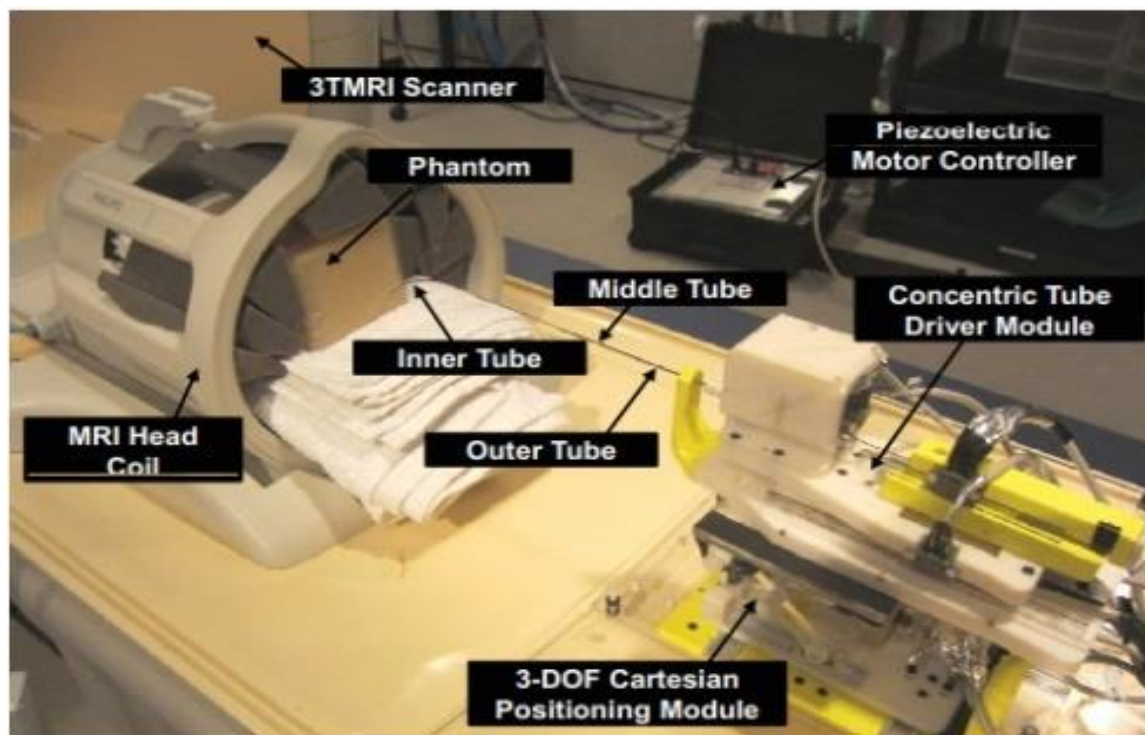
Figure 5 Schematic illustration of piezoelectric actuation robot [40]

IV. Magnetic actuation platform

As lung cancer becomes one of the most prevalent malignancies in the world, the magnetic robotic detection and therapy becomes a hot topic. The magnetic platforms for medical applications are listed in this review. Also mentioned are parameters such as precision, DOF, core components, and fabrication methods. Additionally, the difficulties are described in detail. All of them demonstrate the magnetic robots' potential for usage in healthcare procedures to deliver precise, dependable operations for diagnosis. The development of magnetic guided robots would be promising as more researchers focused on magnetic actuated robot systems.

Soft magnetic actuators have become a transformative force in the field of Minimally Invasive Surgery (MIS), altering the landscape of surgical practices. The adoption of magnetic actuation technologies in MIS has introduced a new era marked by enhanced precision, adaptability, and safety during surgical interventions. This innovative approach enables unparalleled navigation through the vascular system, bronchi, ducts, and similar anatomical pathways, revolutionizing the execution of surgical procedures with its advanced capabilities. This section reviews the magnetic actuation platform and soft magnetic catheter that developed by academic research groups, are explored in terms of their functionality, potential applications, and limitations. Additionally, we delve into the obstacles and future possibilities for integrating magnetic interventional technologies into clinical practice, aiming for widespread acceptance and implementation.
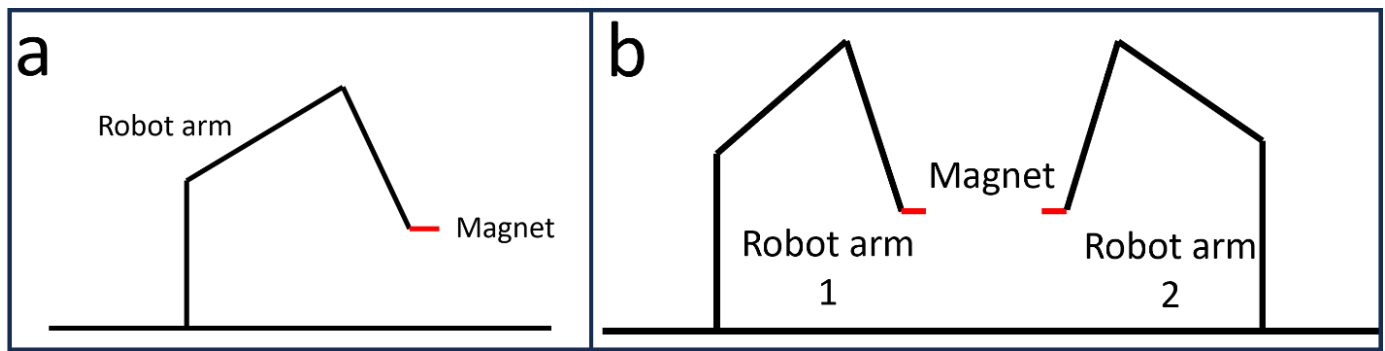
Figure 6 Magnetic actuation platform based on magnet: (a) Single robot arm (b) Dual robot arm

A widely utilized method for generating a magnetic field involves attaching a magnet to the end effector of a robotic arm (Figure 6). This technique takes advantage of the magnet's ability to produce a static and relatively strong magnetic field in outer space without the need for external power sources. Leveraging these properties, Pittiglio et al. [41] developed a dual-arm magnetic actuation platform capable of independently manipulating eight degrees of freedom (DOFs). Despite its advantages, this system is more expensive and complex than single robot arm-based platforms.

Another type of magnetic actuation platform frequently employed by researchers is the electromagnetic-coil system [3, 10, 42-44]. This category includes configurations such as the eight-coil system (Figure 7a) and the three-dimensional Helmholtz coil system (Figure 7b). These systems can generate a precise magnetic field within a limited area, making them suitable for applications requiring high precision. However, their small effective range limits their applicability in surgical contexts. And all of the actuation platform are available in Appendix A.
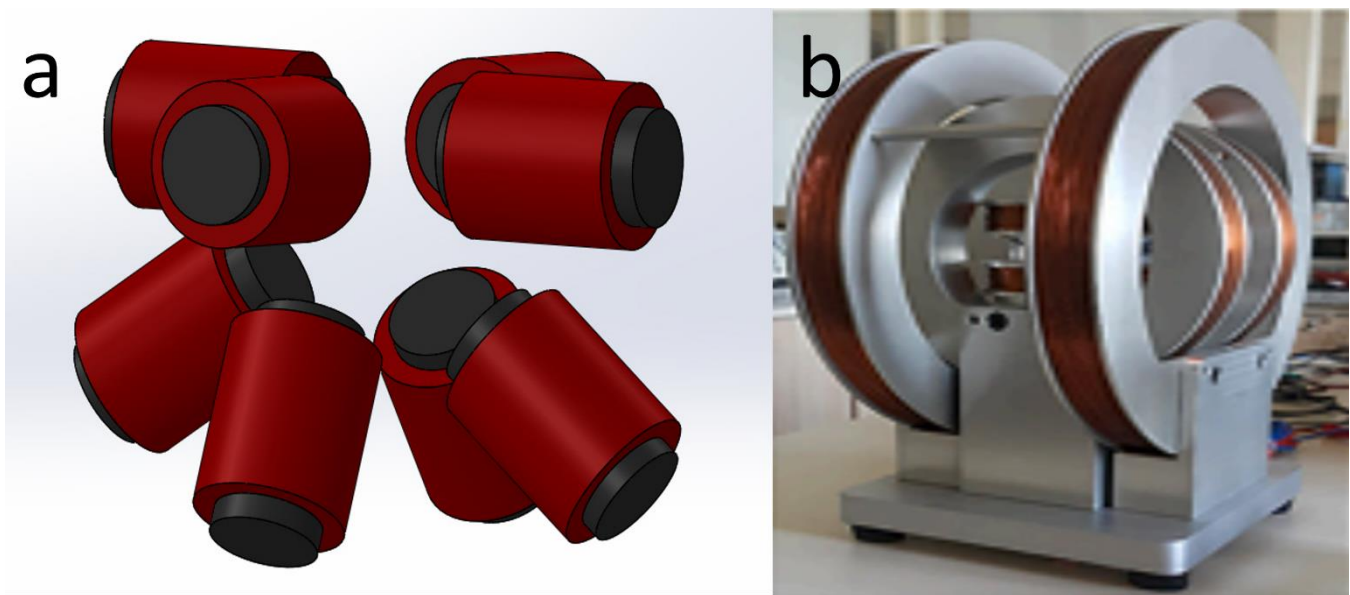

Figure 7 Illustration of different types of magnetic coil: (a) 8 magnetic coil system (b) 3D Helmholtz coil system[45]

In 2009, Ciuti et al. proposed a magnetic actuation platform by fixing a permanent magnet to a robot arm's end-effector to produce the controlled magnetic field[46]. One significant advantage of using permanent magnets is their ability to generate a static and strong magnetic field in outer space without needing external power. Unlike electromagnets, which rely on current-carrying coils and are susceptible to heat loss, permanent magnets avoid these inefficiencies, making them more energy-efficient for producing comparable magnetic field strengths. Electromagnets typically concentrate magnetic flux by arranging multiple coils

around a highly permeable soft-magnetic core. However, a permanent magnet can often produce a magnetic field strength up to an order of magnitude greater than that of an electromagnet of similar size.

Summary and from literature review

The advancement of magnetic actuation platforms and magnetic catheters is discussed in this thesis. Magnetic robots may be used in minimally invasive surgery, according to numerous research. Although these are positive developments for the potential use of magnetic robots in therapeutic settings, various robot systems and actuators have only been tested on animals [9] or phantoms [9, 47, 48], and no clinical applications have been reported. There are still several difficulties preventing the widespread adoption of magnetic actuated robotics that are appropriate for MIS in clinical operation.

One significant challenge in the miniaturization of catheters is the difficulty in maintaining visibility as the catheter size decreases. Reducing the size of soft robots requires the development of cameras with sufficiently small sensors, which are crucial for navigation. Additionally, the size of wireless magnetic capsules is primarily constrained by the battery, which occupies the majority of the available space. Enhancing the dexterity of magnetic catheters while maintaining adequate tissue manipulation capabilities is problematic due to size constraints, limiting the integration of additional manipulators. Moreover, although some magnetic platforms can generate uniform magnetic fields with adjustable direction and strength for controlling magnetic catheters, none can produce continuously varying magnetic fields in space. This limitation restricts the potential applications and maneuverability of magnetic catheters.

Research methodology

This section presents the design, fabrication, and testing of a magnetically actuated soft robot specifically designed for navigation within pulmonary bronchi and blood vessels. The robot features a cylindrical structure with a diameter of 2 mm and a length of 40 mm, composed of a mixture of silicone elastomer and neodymium-iron-boron (NdFeB) particles in a 1:1 weight ratio. This ratio ensures strong magnetic properties while maintaining flexibility. The cylinder is magnetized along its axis using a 5T magnetic field to reduce the magnetic field strength required for actuation or bending. Mathematical modeling was conducted to understand the influence of magnetic particle content, magnetizing field intensity, and external magnetic field strength on the robot's performance. A novel method using cylindrical NdFeB magnets for actuation was introduced, and COMSOL simulations were performed to determine the smallest effective cylindrical magnet size under critical conditions. The fabrication process involved molding the silicone-NdFeB mixture into the desired cylindrical shape and magnetizing it. An accuracy testing platform was developed to evaluate the precision of the robot's movements under an external magnetic field, providing data for optimizing the design and actuation system. In-vitro demonstrations showed the robot successfully navigating to different parts of the pulmonary bronchi using the proposed actuation method, highlighting its potential for medical procedures. The study offers a comprehensive approach to the design, modeling, fabrication, and testing of a magnetically actuated soft robot, demonstrating high precision and effectiveness in navigating complex internal pathways, with future work focusing on refining the design and expanding its clinical applications.
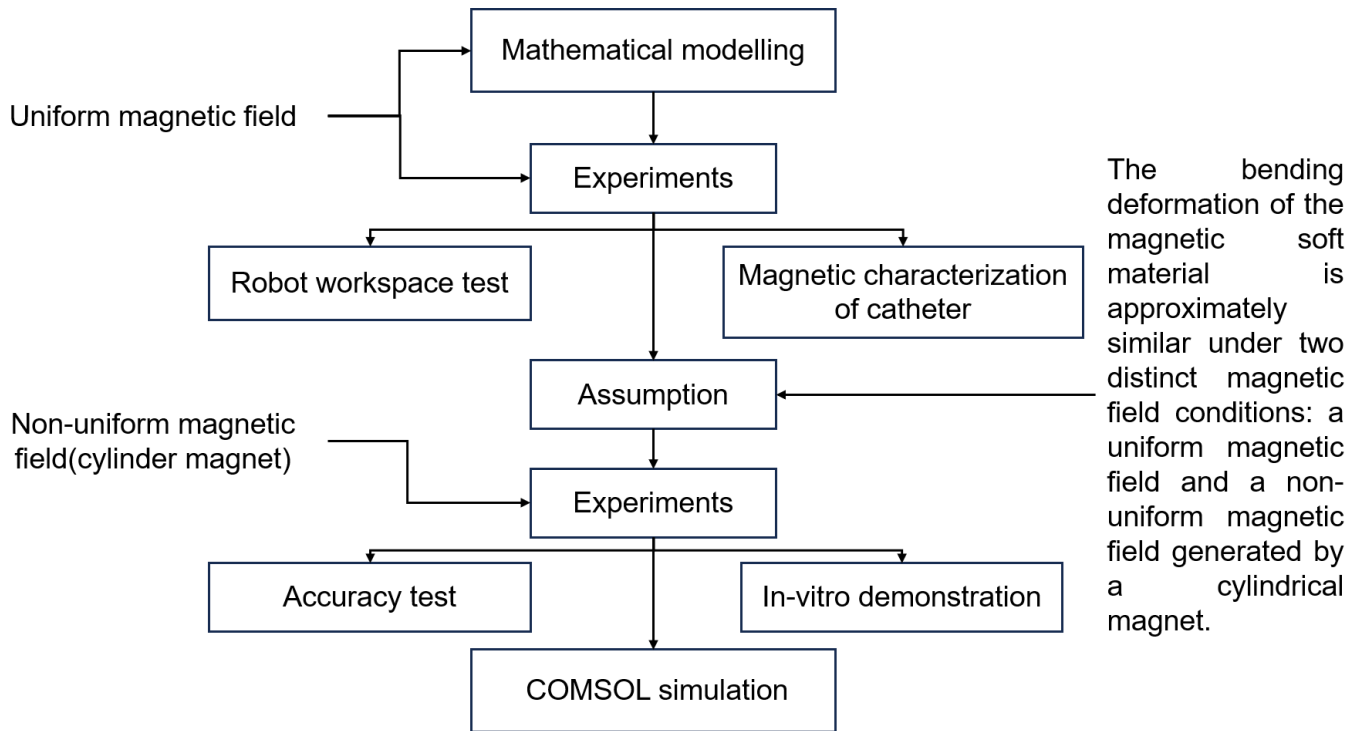
Figure 8: Schematic of the interaction between mathematical modeling, experiments, and COMSOL simulation

As shown in Figure 8, the schematic illustrates the interaction between the mathematical modeling, experimental setup, and COMSOL simulations. The diagram highlights the step-by-step process where the uniform magnetic field is substituted by the non-uniform magnetic field generated by the cylindrical magnet, a critical step in continuing the experimental and simulation work. This substitution is based on the assumption that the bending deformation of the magnetic soft material is approximately similar under both uniform and non-uniform magnetic field conditions, assuming the mean magnetic field strength is equivalent in both scenarios. The rationale behind this assumption is that the primary factor driving the deformation is the overall magnetic field strength experienced by the material. However, this simplification neglects the influence of spatial magnetic field gradients in the non-uniform field, which could affect the deformation behavior. Despite this, the assumption enables a focused investigation into the magneto-mechanical coupling and is validated through a combination of experimental measurements and COMSOL simulations, with the experimental results confirming the hypothesis.

I.   Soft robot fabrication

The soft robot was fabricated using a mixture of Dragon SkinTM 20 Medium (Smooth-On, Europe) and nano neodymium iron boron (NdFeB) particles (Molycorp, MQFPTM-B+) at 100% weight concentration as Dragon SkinTM 20 Medium can only withstand a maximum concentration of 100%. The mixture was cast in a two-piece 3D printed mold (Figure 9), which consists of a top and bottom part. The bottom part has air holes to allow for smooth injection of the mixed material, while the top part has injection holes.

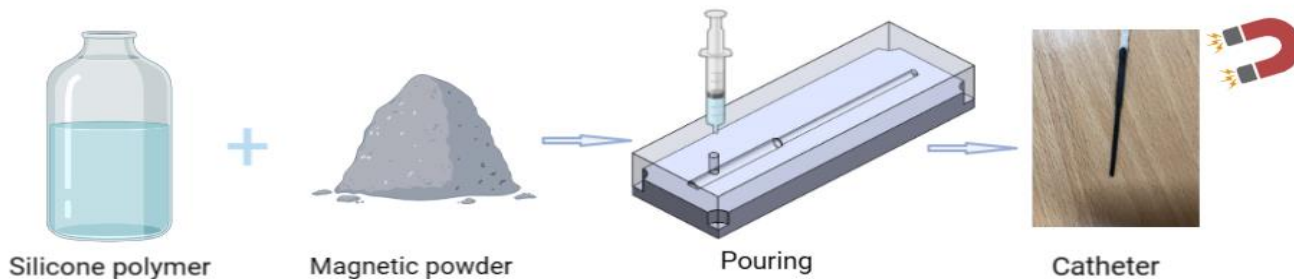Silicone polymer   Magnetic powder   Pouring   Catheter

Figure 9 Illustration of the soft catheter fabrication: The device was created by assembling a mold and preparing a silicone polymer mixture with 5-micron NdFeB particles (MQFPTM-B+, Molycorp, China) at 100% by mass, mixed 1:1 using an ARM-310 mixer (THINKY, USA) at 2000 rpm for 30 seconds. The mixture was poured into the mold, degassed at 0.8 Pa for 20 minutes, sealed, and cured at 60°C for 45 minutes. After curing, the device was magnetized with the IM10-30 (ASC Scientific, USA) and the robot tip was mounted on flexible plastic tubing to form the robot body.

The device was created by first assembling the mold. A silicone polymer mixture was then prepared by mixing NdFeB particles (MQFPTM-B+ magnetic powder, Molycorp, China) with a particle size of 5 microns at 100% by mass in a mixer (ARM-310, THINKY, USA) at a speed of 2000 rpm for 30 seconds, achieving the highest magnetic particle density and ensuring uniform mixing. The mixture, made up of a 1:1 ratio of silicone to NdFeB particles, was poured into a mold cavity and degassed in a vacuum chamber at 0.8 Pa for 20 minutes to remove air bubbles. The top piece of the mold was then mounted to displace any excess polymer, and the cavity was sealed and cured at 60°C for 45 minutes. After curing, the device was taken out of the mold cavity and magnetized with the IM10-30 magnetizer from ASC Scientific (USA), allowing it to be controlled by smaller magnetic fields. The robot tip was subsequently fabricated and attached to flexible plastic tubing, which serves as the body of the robot.

II. Mathematic modelling

Unlike the mathematical models used by other researchers, we include the large bending angle, whereas others ignore it [16], which only be appropriate for small deformations. Let's evaluate the mechanical effect of an external, uniform magnetic field on our soft robot. Let's place the robot in an idealised environment; it will be suspended between two large electromagnets to eliminate the effect of gravity and to obtain a truly uniform magnetic field.
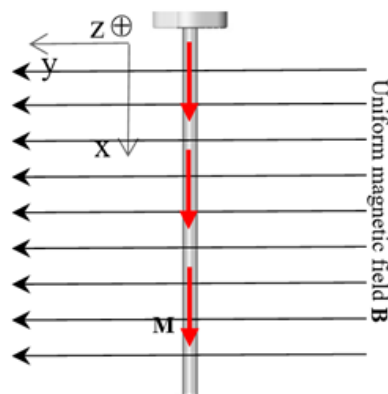

Figure 10 Principle of magnetic actuation

Mathematically, the force (**F**) on a small magnet with magnetic moment m due to a magnetic field B is given by:

$$\mathbf{F} = \nabla(\mathbf{m} \cdot \mathbf{B}) \qquad (1)$$

Here, the gradient ∇ represents the change in the quantity $\mathbf{m} \cdot \mathbf{B}$ per unit distance, and its direction is that of maximum increase of $\mathbf{m} \cdot \mathbf{B}$. The dot product $\mathbf{m} \cdot \mathbf{B} = \mathbf{m}B\cos\theta$, where $\mathbf{m}$ and $\mathbf{B}$ represent the magnitudes of the $\mathbf{m}$ and $\mathbf{B}$ vectors, respectively, and θ is the angle between them.

Mathematically, the torque τ on a small magnet is proportional to both the applied magnetic field and the magnetic moment m of the magnet:

$$\boldsymbol{\tau} = \boldsymbol{m} \times \mathbf{B} = \mu_0 \boldsymbol{m} \times \mathbf{H} \qquad (2)$$

where $\times$ represents the vector cross product. Using the definition of $\mathbf{m}$ as the pole strength times the distance between the poles, this leads to $\tau = \mu_0\, m\, H \sin\theta$, where μ_0 is a constant called the vacuum permeability, measuring $4\pi \times 10^{-7}$ V·s/(A·m), and θ is the angle between $\mathbf{H}$ and $\mathbf{m}$.

However, the gradient ∇ is 0 in the uniform field, hence $\mathbf{F} = 0$, which means that the only contribution of the magnetic field is τ on the cantilever. In our case, the magnetization is done beforehand in the x-direction, so the cross product is simplified to

$$\boldsymbol{\tau} = \boldsymbol{\mu} \times \mathbf{B} = \begin{bmatrix} \hat{\mathbf{x}} & \hat{\mathbf{y}} & \hat{\mathbf{z}} \\ \mu_x & 0 & 0 \\ B_x & B_y & B_z \end{bmatrix} = \mu_x B_y \hat{\mathbf{z}} - \qquad (3)$$

$\mu_x B_z \hat{\mathbf{y}}$

In the first setup of the experiment, we applied the magnetic field in one direction only B_y, so the torque is further simplified to

$$\boldsymbol{\tau} = \mu_x B_y \hat{\mathbf{z}} \qquad (4)$$

The magnetization can be expressed as $m = V_{\text{nano}} \mathbf{M}$, where V_{nano} represents the volume of a single magnetic nanoparticle, $\mathbf{M}$ is the volumetric magnetisation, which is equal to $\mathbf{M} = \chi_v \mathbf{H}$, where χ_v represents the volume magnetic susceptibility. $\mathbf{H}$ is the magnetic field strength in amperes per meter. Using SI units, the magnetic induction $\mathbf{B}$ is related to $\mathbf{H}$ by the relationship.

$$\mathbf{B} = \mu_0(\mathbf{H} + \mathbf{M}) = \mu_0(1 + \chi_v)\mathbf{H} = \mu\mathbf{H} \qquad (5)$$

As the nanoparticle is very small, we can treat it as a point dipole, which results in the susceptibility being negligible. Therefore, if there are N number of nanoparticles in our structure:

$$\mu_x = \frac{B_m}{\mu} NV_{\text{nano}} \qquad (6)$$

To see the relationship between the magnetic field, modulus of elasticity and curvature, let's look at a cantilever fixed at one end. In this case the bending moment M is

$$M = \frac{EI}{\rho} \approx EI \frac{d^2y}{dx^2} \qquad (7)$$

where E is Young's modulus, I is the moment of inertia, ρ is the radius of curvature and y is the displacement of the robot. The bending moment M in our case is $M = \int_x^l \tau\,dx$ where τ is the torque generated by the magnetic torque and I is the length of the robot. The known relationship is $\tau = \mu_x B_y \hat{\mathbf{z}}$. Using this and (7), the bending moment becomes

$$M = \int_x^l \frac{B_m NV_{\text{nano}} B_y \sin\theta}{\mu l}\,dx \qquad (8)$$

where θ is the angle between $\mathbf{B_m}$ and $\mathbf{B_y}$ at each point of the robot.

$$\theta = \arctan\frac{1}{\int M\,dx} \qquad (9)$$

Equating this with (7), (8) and reorganizing:

$$\frac{d^2y}{dx^2} = \frac{B_m NV_n B_y \sin\left(\arctan\dfrac{1}{\int M\,dx}\right)}{EI\mu l} \qquad (10)$$

According to (10), the deformation of the robot is directly proportional to the content of the small magnet and the strength of the applied magnetic field, and inversely proportional to the modulus of elasticity. This equation can serve as a guideline for the design and fabrication of robots.

III. 1-D magnetic characterization of catheter.

The experimental setup, illustrated in Figure 11, was meticulously designed to investigate catheter deflection under various magnetic fields, aiming to enhance medical procedures within the chest cavity. A high-

precision electromagnet, capable of generating stable and uniform magnetic fields up to 0.03 Teslas, suspended the catheter, enabling precise measurement of deflection. A Gaussmeter, positioned adjacent to the catheter's initial location, accurately measured the magnetic field strength. Concurrently, an iPhone (Resolution: 1920 x 1080 pixels, associated optical error: 0.014014mm) captured images of the catheter's deflection at the non-suspended end under different magnetic field strengths. These images were subsequently analyzed using ImageJ software to determine the exact deflection in millimeters. COMSOL Multiphysics was employed to simulate the magnetic field distribution and predict the catheter's behavior under various conditions, providing robust validation for the experimental data. The results, as depicted in Figure 16, demonstrate the relationship between the applied magnetic field and the catheter's deflection, underscoring the efficacy of magnetic field manipulation in medical applications.
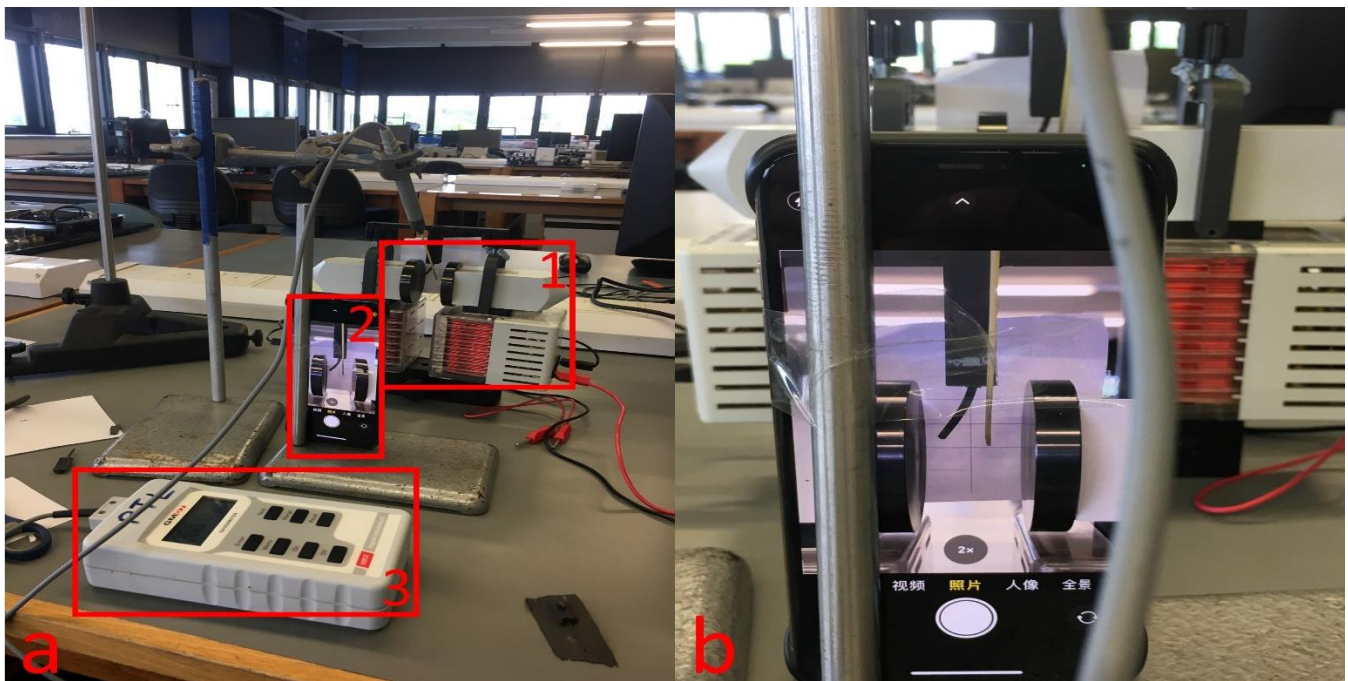

Figure 11 Set up of the 1-D deflection experiment: (a)-1:1-D magnetic coil, (a)-2:Camera that capture the movement of catheter, (a)-3:Gauss meter

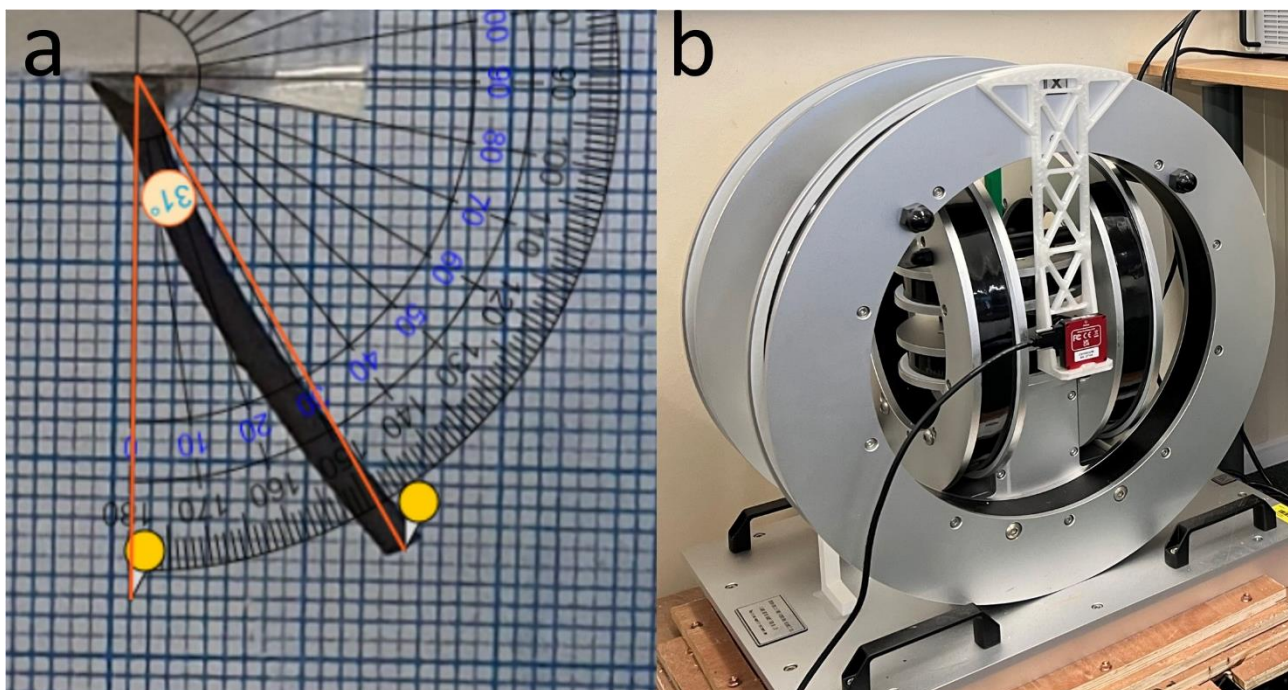# IV.   3-D magnetic characterization of the catheter

Figure 12 Set up the measurement of bending angle: (a) Catheter is placed within the magnetic field (b) A 3-axil magnetic machine is used to provide the magnetic field.

The experiment depicted in Figure 12 involves measuring the bending angle of a catheter within a magnetic field. In Figure 12(a), the catheter is positioned within the magnetic field, and its bending angle is measured using a protractor for demonstration purposes, created using the Ginifab online software. The actual bending angle, determined with reference to a grid for accuracy, is shown as 31 degrees. Orange lines represent the bending angle, while yellow circles indicate specific measurement points on the catheter. Figure 12(b) shows a 3D Helmholtz coil system used to generate the magnetic field required for bending the catheter. This device, equipped with multiple coils, allows precise control of the magnetic field's direction and strength. The setup facilitates the study of the catheter's bending response under various magnetic field conditions, which is crucial for developing magnetic actuation systems for precise control and manipulation of catheters in medical applications.

V.   Working distance and magnet actuation analysis based on COMSOL simulation

To determine the feasibility of this new driving method, that is, whether a magnet can provide a magnetic field of sufficient strength and in any direction at any point within the thoracic cavity. The determination of the shape, size and working distance of the magnet for the steering control of the magnetic catheter is subject to practical considerations due to the working space limitations of the patient's geometry and surrounding objects, as well as the spatial distribution of the magnetic fields around the magnet. A potential working range for the actuating magnet to steer the guidewire was estimated, taking into account the average chest thickness [49] and the anatomical location and orientation of the bronchi (Figure 13 (a)). When navigating the robot within the bronchi, the distance from the magnet's surface to the middle of the chest is considered the farthest area within the bronchi from the actuating magnet. Assuming the magnet is positioned near the chest with appropriate safety margins, this distance is approximately 110 mm, as shown in Figure 13 (a). For navigation from the middle of the lung to the chest or back, the distance between the magnet surface and the guidewire's steerable tip should be less than 110 mm. This distance should decrease as the guidewire advances towards the periphery. The magnetic field applied by the magnet from this range should be strong enough to induce a deflection of the guidewire tip between 0-90 degrees, which requires a magnetic field of 0-20 mT. To ensure this, we characterised the workspace of the steerable tip under the influence of applied magnetic fields (Figure 24 (f)) and field gradients from a single actuating magnet as shown in Figure 13 (b).
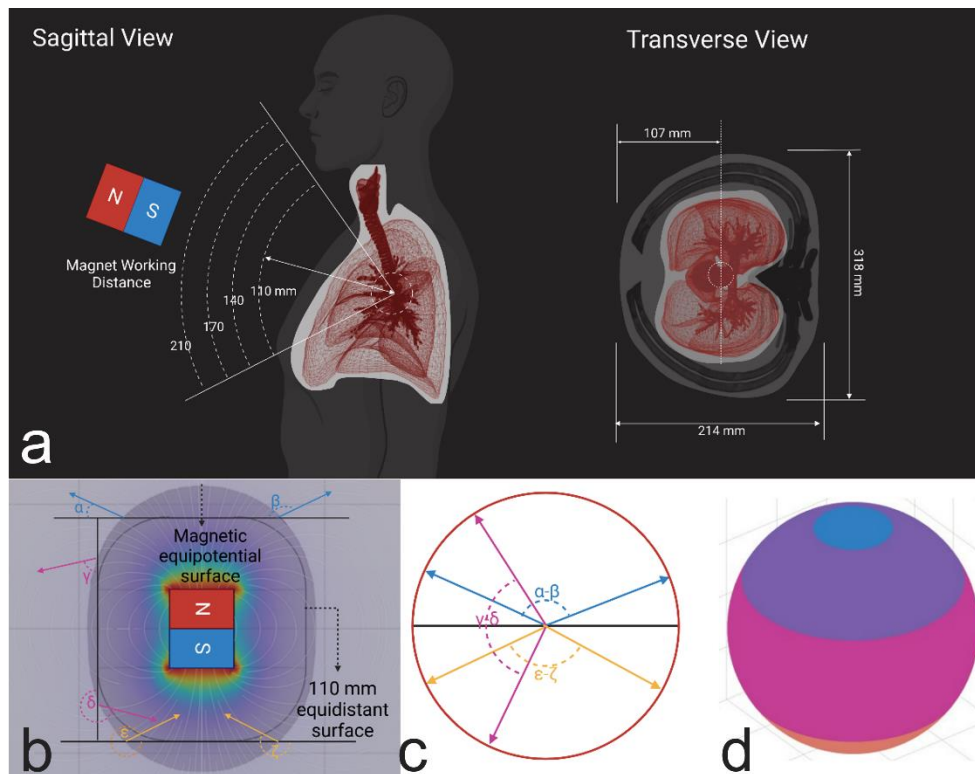

Figure 13 Design considerations for magnetic actuation with a single magnet. (a) Working distance and area for a cylindrical magnet (diameter of 100 mm and thickness of 120 mm) around the chest considering the average chest size[49] and anatomical location and orientation of bronchi illustrated on the sagittal and transverse planes. (b) Illustration of 110 mm working distance and 20 mT magnetic equipotential surface as well as axial usable magnetic field and lateral magnetic field direction and limit angle (α=30.47°, β=149.53°, γ=77.64°, δ=257.64°, ε=329.53°, ζ=210.47°). (c) Set of magnetic field angles: α- β indicate the angle range when N pole of N52 magnet towards the chest and parallel shift can provide (d) Schematic representation of the direction of the magnetic field in three dimension.

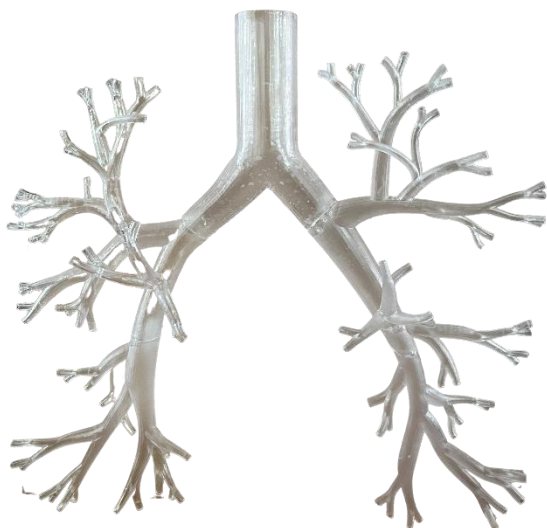# VI.   Accuracy test platform and anatomical lung model

Figure 14 Transparent anatomical lung model (Koken Bronchoscopy Training Model from GT Simulators)

The proposed soft catheter was tested using a Koken Bronchoscopy Training Model (Figure 14) from GT Simulators, which is commonly used for surgical training. The accuracy test platform comprises two cameras (SUNNY OPTICAL TECHNOLOGY, Resolution: 1920 x 1080 pixels, China) that record the catheter's trajectory, two vertical reference papers placed around the catheter to provide coordinates, and a robot arm (Ned2, NIRYO, France) holding a permanent magnet (FINDMAG, FD-M40X20) to control the catheter's movement, as shown in Figure 15(a). The catheter and coordinate system were captured using a SUNNY OPTICAL TECHNOLOGY camera (Resolution: 1920 x 1080 pixels) from China, positioned 50 cm away from the catheter. To ensure consistent lighting conditions, a standard light source was placed to the right of the camera. ImageJ[50] was utilized to calibrate the reference coordinate system and measure the catheter tip's location in each captured image. The catheter tip positions were then plotted in MATLAB to generate a 3D graph of its trajectory relative to the reference coordinate system.
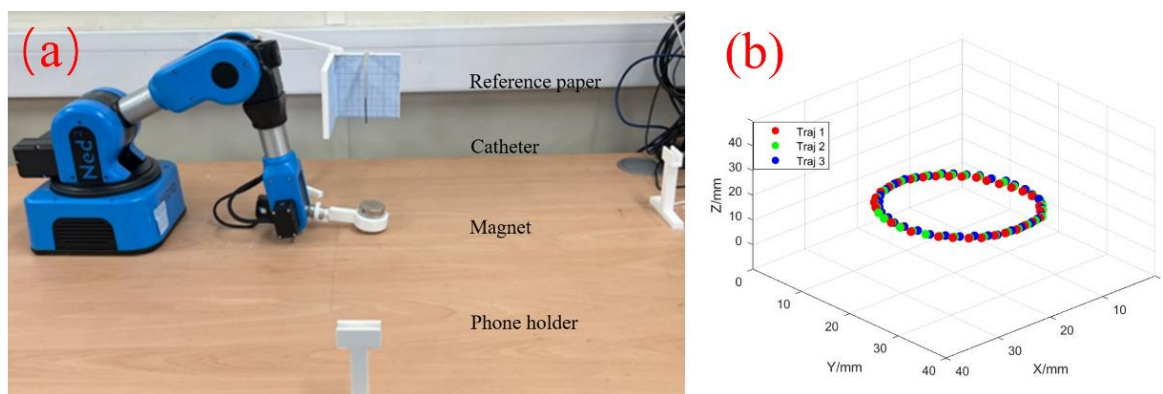

Figure 15 Illustration of the accuracy test platform(a) and result(b)

Results

I.   1-D magnetic characterization of catheter.
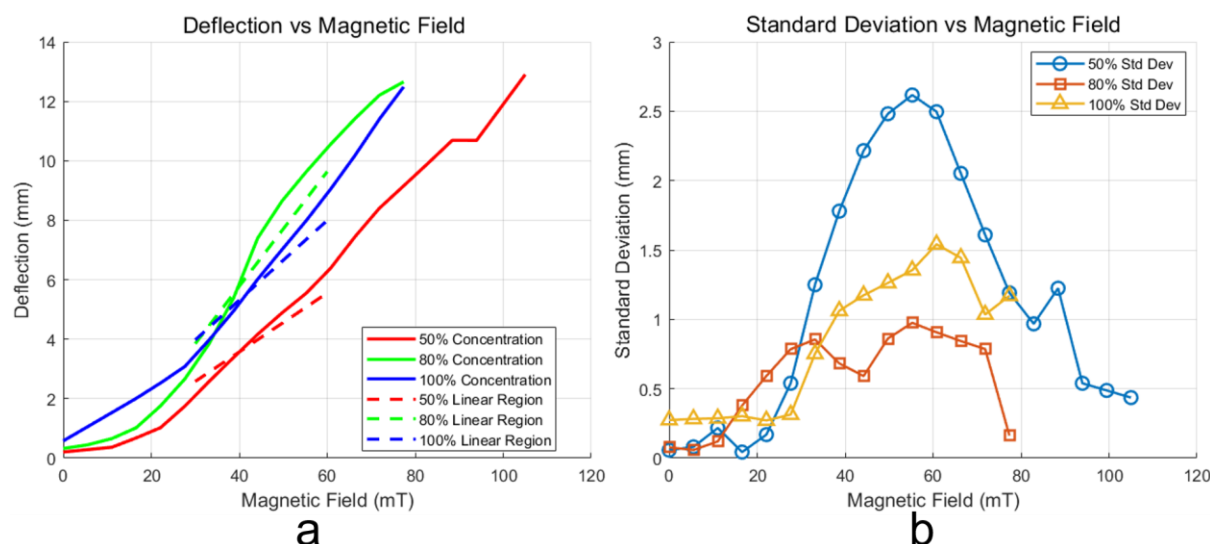

Figure 16 The deflection of three catheters with microparticle weight concentrations of 50%. 80% and 100%

It is apparent from Figure 16 that the higher the microparticle concentration, the lower minimum magnetic field we need to start the deflection. This minimum threshold magnetic field does not appear in the theoretical model. However, the linearity, at least in a region as show in Figure 16a, is apparent the deflection of the robot follows the magnetic eld increment in a linear fashion. At high fields the linearity is not so obvious. An explanation for this could be that the linear relationship model assumes, namely that the deflection angle is small. At higher magnetic fields the deflection angle reaches around 20 degrees or more making the initial assumption false. In the linear section the gradient of the functions could be used to determine the unknown Young's modulus by using Equation (10). Using the values gained from these backward calculations in the COMSOL model gave us a probable value of Young's modulus. When plotting deflection-field relationships in COMSOL, however, the plotted functions weren't even close to the experimental results. The possible reason for the significant discrepancy between your COMSOL simulations and experimental results could be the assumption of small deformations in the simulation. However, in the experimental setup, the magnetic soft material undergoes large deformations. These large deformations make it difficult to ignore the effects of the deformation, which causes the two magnetic field directions to no longer remain perpendicular. This could explain why the experimental results deviate from the simulations.
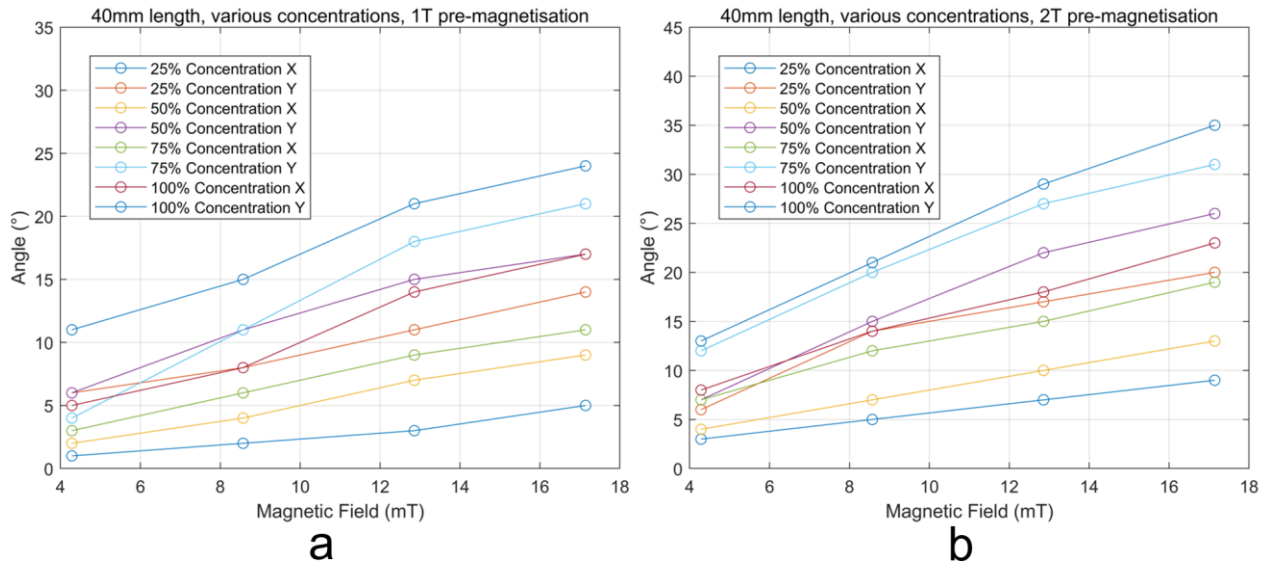
II.   3-D magnetic characterization of catheter

Figure 17This chart displays experimental results under two different conditions, with each graph showing the variation of angle (°) with different concentrations at various voltages (V), The left(a) and right(b) graphs represent the conditions of 1T and 2T pre-magnetization
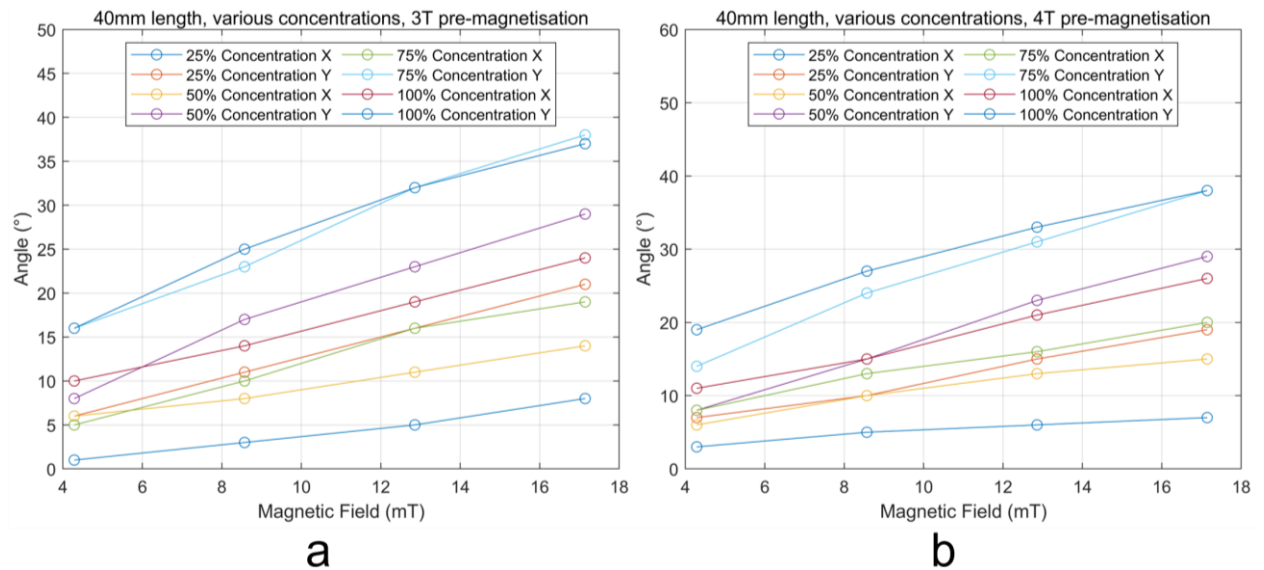

Figure 18 This chart displays experimental results under two additional conditions, with each graph showing the variation of angle (°) with different concentrations at various voltages (V). The left(a) and right(b) graphs represent the conditions of 3T and 4T pre-magnetization
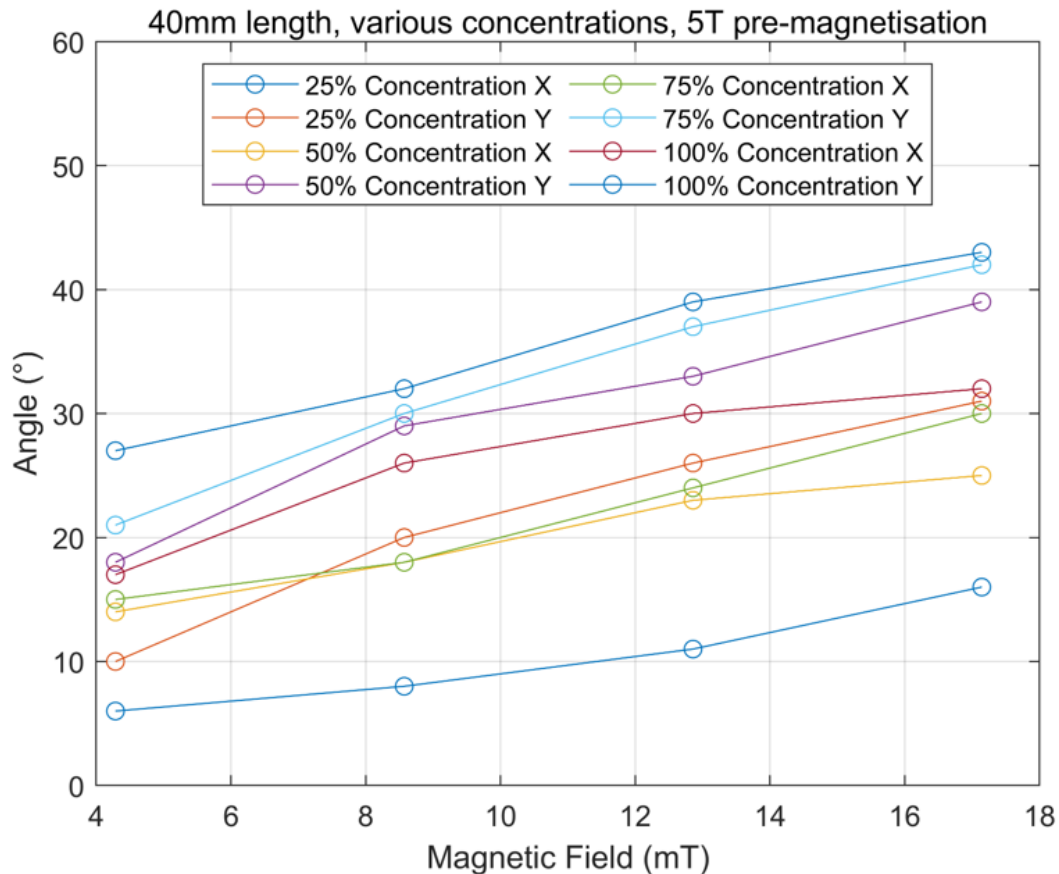
Chengdong Xu

Figure 19 This chart presents the experimental results under the condition of 5T pre-magnetization. It shows the variation of angle (°) with different concentrations at various voltages (V).

The results demonstrate the relationship between angle (°) and voltage (V) for different concentrations under various pre-magnetization strengths (1T, 2T, 3T, 4T, and 5T). As the voltage increases, the angle consistently increases across all levels of pre-magnetization and concentrations. Higher pre-magnetization strengths result in more significant angle changes, with the most substantial variations observed at 5T pre-magnetization. Additionally, higher concentrations correspond to steeper increases in angle with increasing voltage, particularly in the X direction compared to the Y and Z directions.

Specifically, under 1T pre-magnetization, the angle changes are relatively small, with more pronounced changes in the X direction than in the Y direction. This trend intensifies with increasing pre-magnetization strength (2T, 3T, and 4T), leading to progressively larger angle changes. At 5T pre-magnetization, the angle changes are the most substantial, with significant increases observed in all directions, especially the X direction.

These findings indicate that both pre-magnetization strength and concentration significantly affect the angle changes in the material under different voltages. Higher pre-magnetization strengths and concentrations lead to more pronounced angle variations, highlighting the importance of these factors in influencing the material's response to applied voltage.
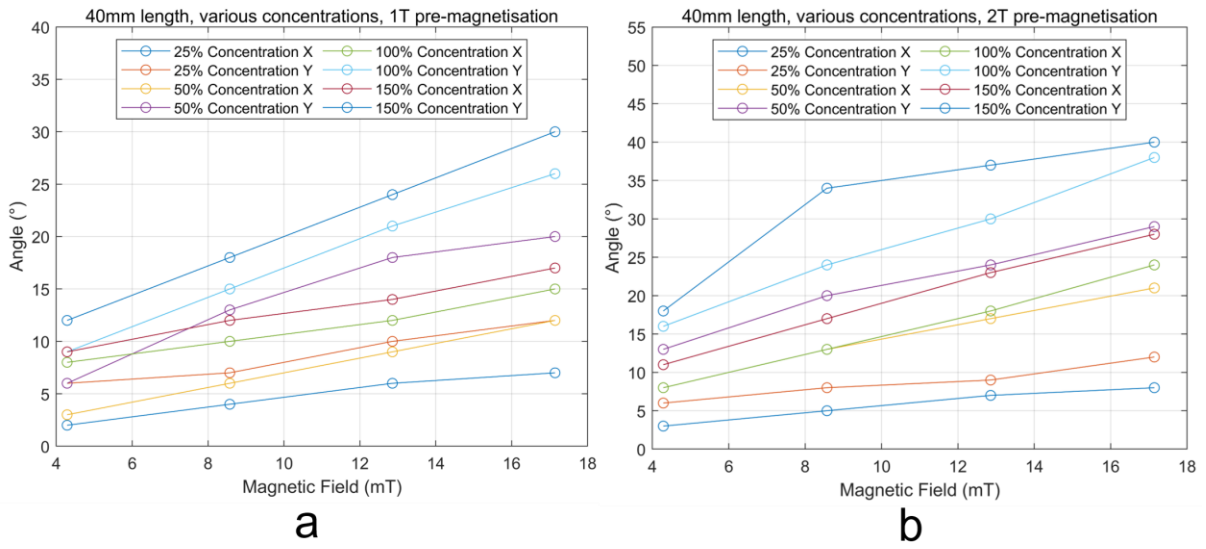
Figure 20This chart displays experimental results under two different conditions, with each graph showing the variation of angle (°) with different concentrations at various voltages (V), The left(a) and right(b) graphs represent the conditions of 1T and 2T pre-magnetization
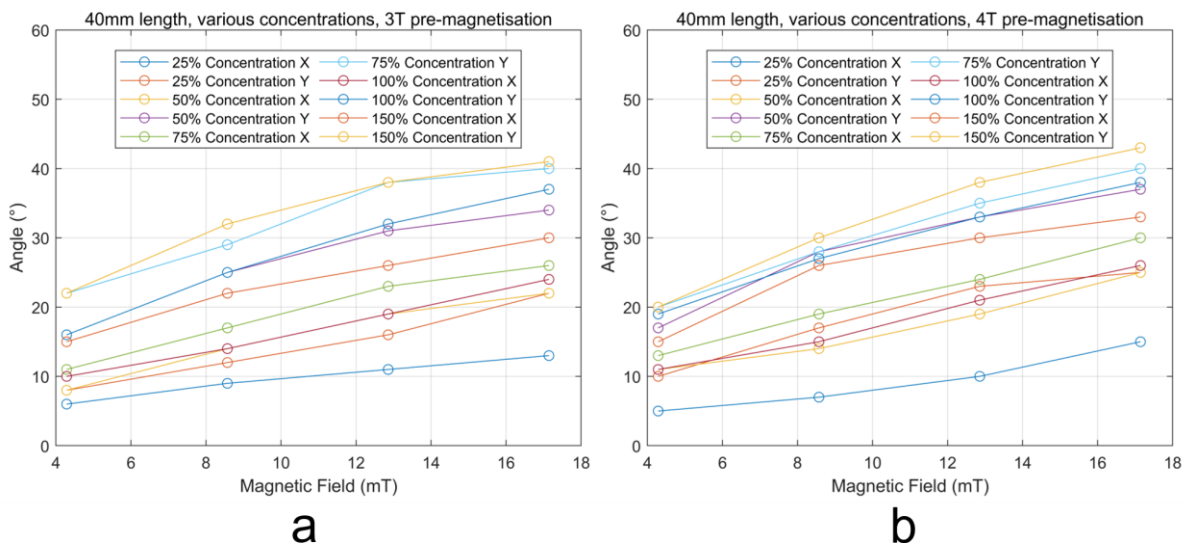

Figure 21This chart displays experimental results under two different conditions, with each graph showing the variation of angle (°) with different concentrations at various voltages (V), The left(a) and right(b) graphs represent the conditions of 3T and 4T pre-magnetization
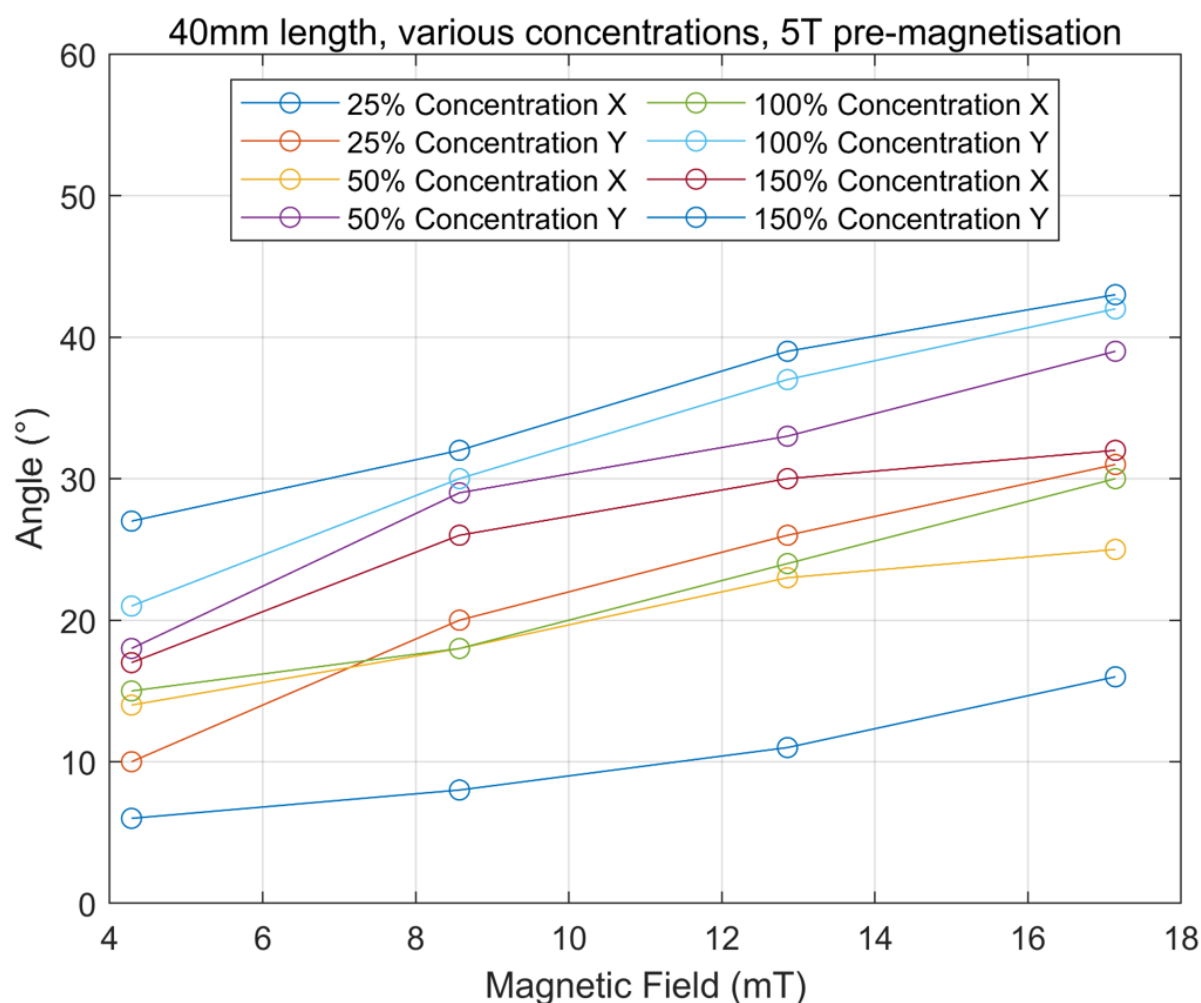
Figure 22 This chart presents the experimental results under the condition of 5T pre-magnetization. It shows the variation of angle (°) with different concentrations at various voltages (V).

The presented figures collectively illustrate the experimental outcomes under varying pre-magnetization conditions (Ecoflex 30), showing the relationship between angle (°), concentration, and voltage (V). Figures 18 and 19 compare different pre-magnetization strengths, with Figure 18 focusing on 1T and 2T conditions and Figure 19 on 3T and 4T conditions. Both sets of data reveal a consistent trend: the angle increases with higher concentrations and voltages, underscoring the magnetic response's dependency on these variables. Figure 22, which isolates the 5T pre-magnetization condition, further corroborates this trend, showing an amplified angle variation under stronger magnetic fields. Collectively, these results underscore the significant influence of pre-magnetization strength on the material's magnetic properties, highlighting a positive correlation between angle, concentration, and voltage across all tested conditions. This analysis provides critical insights into how pre-magnetization can be leveraged to modulate magnetic responses for various applications, showcasing a clear pattern of enhanced magnetic behavior with increasing field strength.

The analysis of the measurements obtained from the study of catheter bending under the influence of various parameters reveals several key findings. Firstly, the concentration of magnetic particles, the level of pre-magnetization, and the voltage delivered to the coils significantly impact the catheter's ability to bend. Higher concentrations of magnetic particles

and higher pre-magnetization values align the magnetic moments of the particles more effectively, resulting in a stronger reaction to the magnetic field and thus a greater bending angle. Similarly, higher voltages in the coils create stronger magnetic fields, enhancing the catheter's bending capacity. The nature of the catheter material also plays a crucial role; more elastic materials like EcoFlex00-30 enable greater bending compared to more rigid materials like Dragon Skin 10. Among the studied parameters, the concentration of magnetic particles has the most pronounced effect on the bending angle, more so than the pre-magnetization value, indicating its greater importance in achieving desired curvature. The voltage in the coils is also critical, with measured values showing significant increases in bending angles as voltage increases from 3 to 12V. The type of silicone used is another significant factor, with EcoFlex 00-30 silicone consistently resulting in angles 2 to 6 degrees greater than those made from Dragon Skin 10. Optimization of these parameters is essential, and the experiments constrained to specific ranges (length: 40 mm, diameter: 2 mm, voltage: 3 to 12 V, magnetic particles: 0 to 100%, two types of silicone, and pre-magnetization: 1 to 5 T) indicate that the optimal curvature is achieved by maximizing the parameters related to the magnetic phenomenon, including magnetic particle richness, pre-magnetization, and coil tension.

The primary sources of error in the angular measurement include manual measurement uncertainty and pixel resolution limitations. The manual measurement error was estimated as 0.1708° based on repeated measurements (Table 8) of the same angle. The pixel resolution error was calculated by considering the field of view and resolution of the camera. Assuming a horizontal FOV of 60°, a resolution of 1920×1080 pixels, and a camera-object distance of 400 mm, the pixel size was estimated to be 0.69 mm, resulting in an angular error of approximately 0.0988°. By treating these errors as independent and applying error propagation, the total angular measurement uncertainty was determined to be 0.197°. This result highlights the accuracy of the measurement system under the specified conditions.

The experiment provides preliminary insights into the effects of magnetizing the magnetic soft robot with a stronger magnetic field, demonstrating that its magnetic properties can be enhanced as a result. Additionally, an increase in the magnetic particle content within the soft robot facilitates greater deformation, making it more responsive to the applied magnetic field generated by a cylindrical magnet. Based on the findings of a single experimental trial, while these results offer a foundation for understanding the method of driving magnetic soft robots using cylindrical magnets, the lack of multiple trials limits the ability to generalize the conclusions. Future research should focus on conducting repeated experiments to enhance reproducibility and further explore the influence of magnetic particle content and magnetic field strength on the robot's deformation behavior.

III.   COMSOL simulation

Just as before, in the COMSOL Multiphysics® software, we constructed a cylindrical magnet using neodymium iron boron (NdFeB) as the magnet material. This model includes an equidistant surface from the magnet's surface and another surface where the magnetic field strength is equal, as illustrated in Figure 13(b). To ensure that the magnet can provide a sufficiently strong magnetic field to drive a robot in the deepest part of the lungs, i.e., the center of the lungs, we positioned the surface where the magnetic field strength is equal outside the equidistant surface. The distance from the magnet's surface to the equidistant surface was set at 11 cm. To maximize the utilization of the magnetic field from a magnet of the same volume,

we applied the method shown in Figure 3, in combination with the relationship between the equidistant surface and the surface of equal magnetic field strength shown in Figure 13(b), along with the limiting angles of the magnetic field lines α, β, γ, δ, ε, ζ. Through these parameters, we can deduce, as shown in Figure 13c, that when γ is not less than a certain value ' α ', the magnet can provide the required field strength in any direction to the deepest part of the lung, as depicted in Figure 13(d). So that COMSOL simulations were conducted to identify the minimum effective size of the cylindrical magnet under critical conditions. Figure 23 illustrates the relationship between the height of a magnet and the mini-working distance(the distance between magnet and skin of the chest) to the chest, considering different radii (R=8 cm, R=9 cm, R=10 cm) and axes (Minor Axis and Major Axis: Figure 26) and all of the COMSOL simulation results are available in the Appendix B. The data reveals a consistent trend across all radii and axes: as the magnet's height increases, the mini-working distance to the chest generally increases, transitioning from negative values at lower heights to positive values at higher heights (Figure 23 (a)). This indicates that the magnet initially moves closer to the chest and then progressively moves away. Notably, the major axis consistently shows greater distances compared to the minor axis. Specifically, at a height of 0 cm, the mini-working distance is approximately -10 cm for all configurations. The maximum distances observed are around 7 cm for R=8 cm, 10 cm for R=9 cm, and 15 cm for R=10 cm (Figure 23). These findings provide crucial insights into how varying the height and radius of a magnet influences its spatial relationship with the chest, which could be pivotal for applications requiring precise magnetic positioning. The findings indicate that appropriately increasing both the height and width of the magnet can enhance the magnetic field strength and expand its range. However, if the ratio of height to width becomes large than 2, the effectiveness of the magnetic field decreases. Therefore, when designing and applying cylindrical magnets, it is crucial to balance the height and width to ensure optimal magnetic field strength and coverage.

Proper geometric optimization and suitable size proportions are essential for achieving efficient magnetic field distribution.
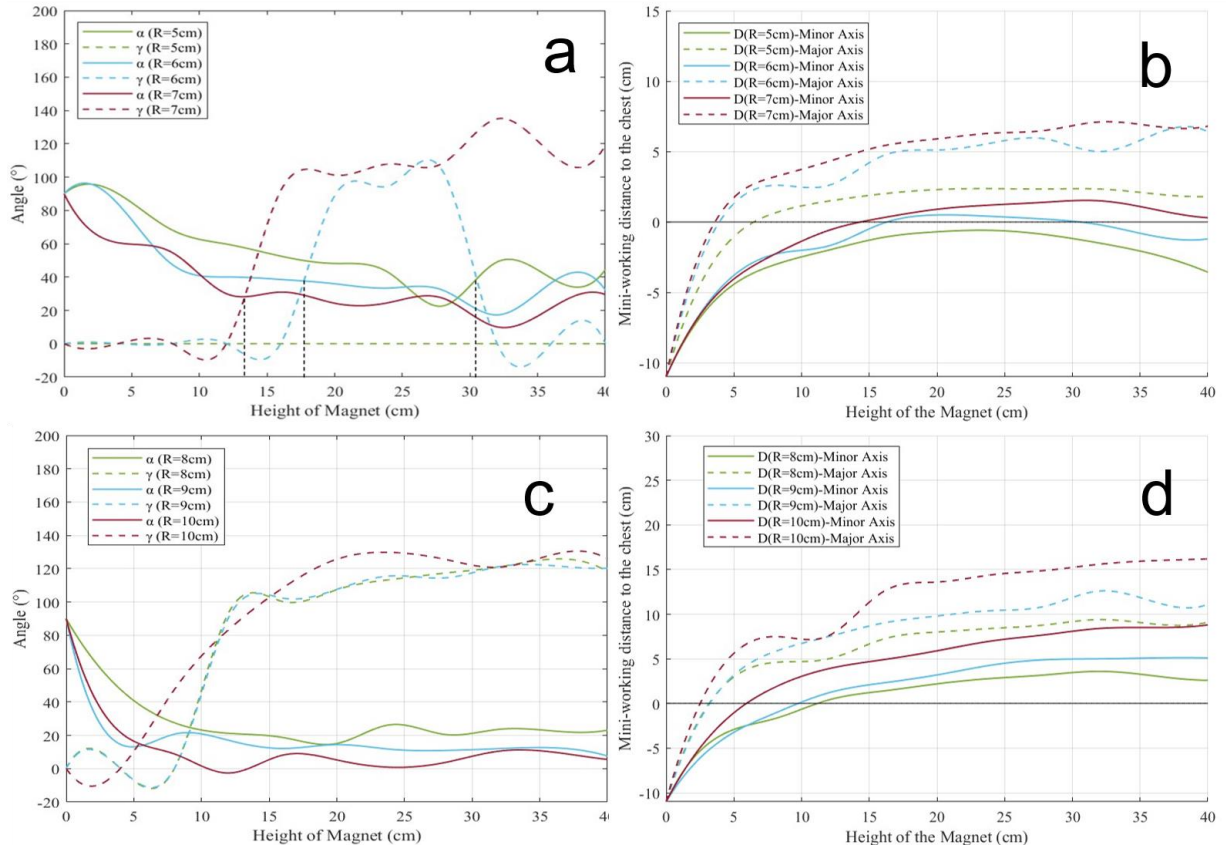

Figure 23 The relationship between Height & Radius of cylinder magnet and working distance & magnetic field angles: α, γ : (a) The relationship between the height of a magnet (in cm) and the mini-working distance to the chest (in cm) for different magnet radii (R=5 cm, R=6 cm, R=7 cm) and axes (Major Axis and Minor Axis). (b) The relationship between the height of a magnet (in cm) and the angle (in degrees) for different magnet radii (R=5 cm, R=6 cm, R=7 cm) and angles (α and γ) (c) The height of a magnet (in cm) and the mini-working distance to the chest (in cm) for different magnet radii (R=8 cm, R=9 cm, R=10 cm) and axes (Minor Axis and Major Axis)(d) The relationship between the height of a magnet (in cm) and the angle (in degrees) for different magnet radii (R=8 cm, R=9 cm, R=10 cm) and angles (α and γ)

IV. Accuracy test

To determine the coordinates of the catheter tip during the circular trajectory of a robot arm equipped with a moving permanent magnet, we used a 3D-printed reference coordinate system, as shown in Figure 15. This involved utilizing ImageJ and MATLAB (MathWorks, USA). The reference coordinate system was established with three orthogonal axes marked in millimeters on two sheets of paper, with the origin located at the lower-left corner. To align the catheter with this coordinate system, it was necessary to centre it on the origin and ensure that it remained parallel to the axes.

The catheter and coordinate system were captured using a camera (SUNNY OPTICAL TECNOLOGY, Resolution: 1920 x 1080 pixels, China) positioned 50cm away from the catheter. To ensure consistent lighting conditions, a standard light source was placed to the right of the camera. ImageJ was used to calibrate the reference coordinate system and measure the catheter tip's location in each captured image. The catheter tip positions were plotted in MATLAB to create a 3D graph of its trajectory relative to the reference coordinate

system.

The data presented in Figure 15(b) highlights the impressive performance of the magnetic catheter during actuation, revealing a maximum accuracy of 0.6 ± 0.32 mm, which is significantly better than others that have an accuracy of more than 1mm[3, 5, 12]. This level of precision, which is only 1.5% of the catheter's initial length (40 mm), demonstrates the robust capabilities of the proposed magnetic catheter system.

The magnetic catheter is a reliable and valuable instrument for medical professionals engaged in bronchial exploration due to its high accuracy. The findings indicate that this innovative tool has the potential to significantly enhance the diagnostic and therapeutic aspects of bronchoscopy. The magnetic catheter holds promise for improving the overall quality and success of medical procedures in the bronchi by providing doctors with a precise and effective means of navigation.
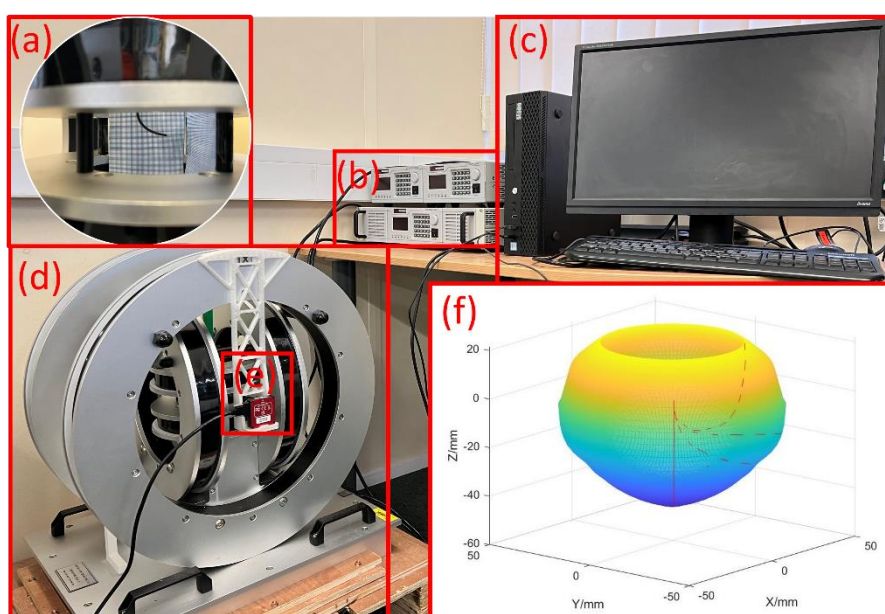
V. Robot workspace

Figure 24Robot workspace test experiment set up as well as result. (a) Photo taken by camera, (b) 3 power supplies for Helmholtz coils, (c) Monitor and computer, (d) 3D Helmholtz coil: Range from 0mT-34mT, (e) Camera, (f) Robot workspace.

To investigate the bending of the robot when applying a uniform magnetic field, we used a printed reference coordinate system, ImageJ, and MATLAB. A 3-axial electric magnet was used to create a uniform magnetic field, as shown in Figure 24(d). The reference coordinate system consisted of three orthogonal axes marked in millimeters on two sheets of paper, with the origin located at the lower left corner of the paper. The catheter was aligned with the coordinate system by centering it on the origin and ensuring that it was parallel to the axes. To capture images of the catheter and coordinate system, we used a camera (SUNNY OPTICAL TECNOLOGY, Resolution: 1920 x 1080 pixels, China) positioned at 40cm from the catheter, with a standard light source located to the right of the camera to ensure consistent lighting conditions. Using ImageJ, we calibrated the reference coordinate system and measured the location of the catheter's tip in each image captured. The positions of the catheter's tip relative to the reference coordinate system were then plotted in MATLAB (MathWorks, USA) to create a 3D graph of the catheter's workspace as shown in Figure 24(f).

To ensure accurate measurements when evaluating the bending behavior of the robot under a uniform magnetic field, a comprehensive assessment of potential error sources was

conducted. The primary sources of error include lens distortion, image resolution limitations, calibration inaccuracies, reprojection error, and manual measurement uncertainty. To evaluate and quantify errors introduced by the camera, a calibration procedure was conducted using MATLAB's Camera Calibrator App and the checkerboard method. A checkerboard pattern with a known square size of 6mm was imaged from multiple angles and orientations to ensure robust parameter estimation. MATLAB's detectCheckerboardPoints function detected the corner points of the pattern, and the estimateCameraParameters function calculated the intrinsic and extrinsic parameters of the camera. The calibration results included an image resolution of 1920 × 1080 pixels, radial distortion coefficients of [0.3346, -2.0432], and no significant tangential distortion (coefficients: [0, 0]). The focal length and principal point were determined to be [3.6737 × 10³, 3.6925 × 10³] pixels and [548.1801, 984.4574] pixels, respectively. The calibration accuracy was evaluated using the mean reprojection error, calculated as 0.1525 pixels (each pixel corresponds to 0.014014mm), indicating high reliability. In addition, the calibration error was quantified by repeatedly measuring 6mm reference distance and calculating the standard deviation(0.0071mm) as show in Table 7. Manual measurement error was quantified by repeatedly measuring the same points and using the standard deviation(0.279mm) as an estimate of uncertainty (

Table 8). Finally, assuming that these errors are independent of each other, we use error propagation to calculate the combined measurement uncertainty: $\Delta_{total} = \sqrt{(\Delta_{calibration\text{-}board})^2 + (\Delta_{manual})^2 + (\Delta_{distortion})^2 + (\Delta_{resolution\text{-}reprojection})^2} = 0.280\text{mm}.$ This estimate of the overall uncertainty demonstrates the reliability of our experimental data by quantifying the measurement accuracy of our device.

The considerable deviation observed in the trajectory of the catheter, as evidenced by our findings, accentuates the dynamic influence exerted by magnetic forces on its structural alignment. Particularly noteworthy is the heightened curvature manifested when the catheter is precisely aligned with the z-axis of the magnetic field, as depicted in Figure 24(f). The commendable curvature and expansive operational space collectively enable proficient navigation of the robot within the pulmonary bronchus. In comparison to alternative magnetic actuation devices and divergent approaches to bronchoscopy, our robot demonstrates a superior proven workspace, as delineated in Table 1.

Table 1 Comparative list of workspace

Author	Actuation	Length	Spherical coverage	Application
Tieshan Zhang[51]	Hybrid	2cm	Hemispherical	MIS
Max McCandless[52]	Air	1cm	Less than 1/8 spherical	Bronchoscopy
Yoonho Kim[9]	Magnetic	N/A	N/A	Neurovascular interventions
Janis Edelmann[3]	Magnetic	13cm	Less than ½ spherical/20mm	Cardiac ablation
Peter Lloyd[10]	Magnetic	5cm	N/A	MIS
Ours	Magnetic	4cm	More than hemispherical	Bronchoscopy

VI.   In-vitro demonstrations

Figure 25 provide a comprehensive visual account of the magnetic soft robot's adept navigation as it successfully reaches the distal end of a bronchial model, and the results of each attempt were placed on the same picture of the transparent model. This remarkable

32

navigational achievement is made possible by harnessing the magnetic fields generated by a handheld permanent magnet (FINDMAG, FD-M40X20). The experimental results show that the robot can navigate in any direction in the model as demonstrated above, especially at large angles upwards.
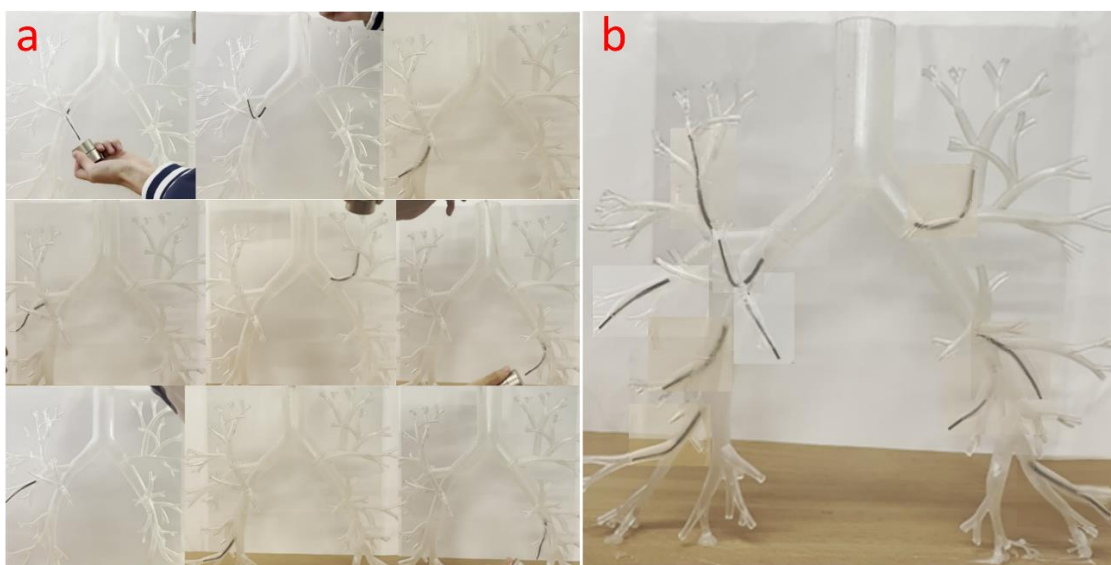

Figure 25 Robot navigation in-vitro: (a) navigation through different path, (b) different result in one graph

The inherent precision and dexterity exhibited by the robot in navigating the complex pathways within the bronchial model underscore the effectiveness of the magnetic control mechanism. This innovative approach not only allows for targeted and controlled movement but also demonstrates the potential applicability of magnetic soft robots in navigating challenging anatomical structures for various medical and industrial purposes.

This rigorous approach not only validates the reproducibility of the results but also emphasizes the reliability of the magnetic soft robot's performance in navigating intricate environments. The successful navigation showcased in the figures holds promising implications for advancing the field of robotic-assisted procedures, particularly in scenarios with complex and constrained pathways.

Conclusion and Future work

This article presents a proposed catheter that offers improved dexterity and a larger tip workspace, making it easier to navigate during bronchoscopy. Additionally, we have developed a new mathematical model that accounts for bending angles beyond small deflections, enhancing its applicability. Simulations of the magnetic field strength and distribution of an N52 magnet were performed, determining the optimal working distance (more than 110 mm) for controlling the catheter within the lung depth with a magnetic field strength of 0-20 mT, which is lower than that reported by other investigators. The larger workspace allows the catheter to bend in any direction within the 0-20 mT magnetic field range, increasing its dexterity and enabling control by a magnet positioned 110 mm away.
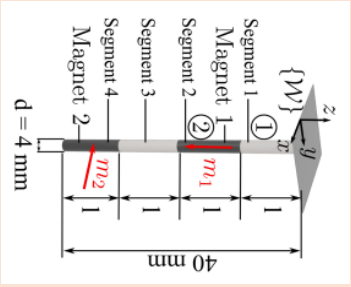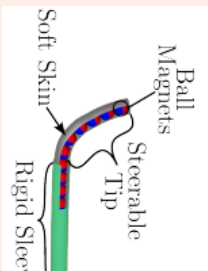
Furthermore, our research included an analysis of the mini-working distance to the chest as a function of the magnet's height, considering different radii (R=8 cm, R=9 cm, R=10 cm) and axes (Minor Axis and Major Axis). The data revealed a consistent trend across all configurations: as the magnet's height increases, the mini-working distance generally transitions from negative to positive values, indicating initial proximity to the chest followed by
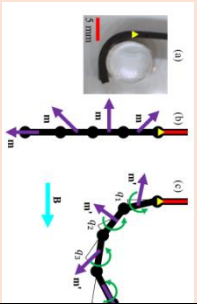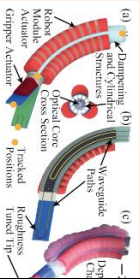
increasing distance. The major axis consistently exhibited greater distances compared to the minor axis, with maximum distances observed at approximately 7 cm for R=8 cm, 10 cm for R=9 cm, and 15 cm for R=10 cm. These findings are pivotal for optimizing the spatial relationship between the magnet and the chest, thereby enhancing the catheter's navigational capabilities.
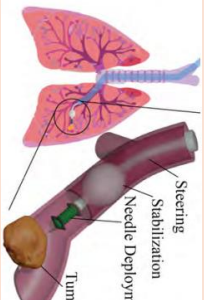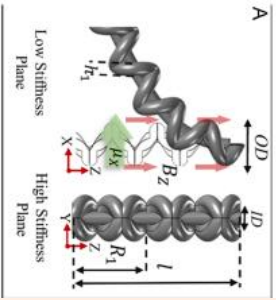
In practice, this optimized setup facilitated the complete navigation of ten primary lumens in the bronchi of an anatomically accurate phantom. The combined improvements in catheter dexterity, mathematical modelling, and spatial optimization underscore the catheter's potential for advanced bronchoscopic procedures, offering a significant enhancement over existing methodologies.
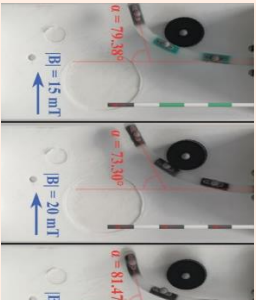
A. Appendix

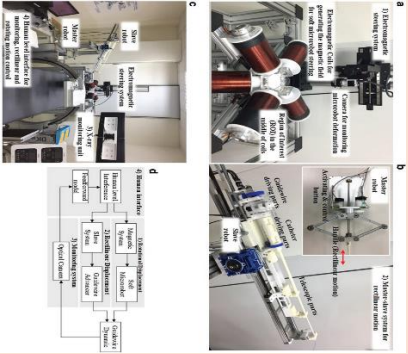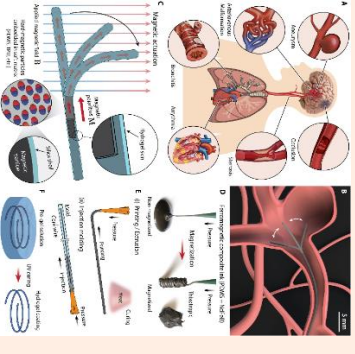| Article title	Compare to our work	Advantages	Disadvantages
Closed Loop Static Control of Multi-Magnet Soft Continuum Robots[54]	The multi-magnet soft continuum robot consists of two magnetically doped segments alternating with magnetically inert segments, each with a diameter of 4 mm. This design incorporates a fiber Bragg grating (FBG) sensor along the main axis of the robot for precise measurement and control. Compared to our thesis, the robot in this paper has a larger diameter, making it unsuitable for narrow spaces less than 4mm.	This model operates in a closed loop at approximately 300 Hz, significantly faster than the 1 Hz and 20 Hz frequencies of previously proposed approaches. The inclusion of a fiber Bragg grating (FBG) sensor enables precise measurements. By accounting for gravity and elasticity, the proposed controller reduces the average error by 20.8% compared to the PID control method.	The FBG sensor limits the degrees of freedom that can be controlled. Instabilities have been observed when the applied magnetic field induces twisting in the upper internal permanent magnet. In such cases, the FBG sensors cannot detect these torsional deformations, leading to the controller being unaware of the actual state of the soft magnetic continuum robot. Consequently, this results in a higher error when attempting to control the robot's desired position.
Closed-form Kinematic Model and Workspace Characterization for Magnetic Ball Chain Robots[53]	The adjustable tip consists of a chain of 10 spherical permanent magnets, all enclosed within a thin, flexible cylindrical skin. Compared to our work, the robot in this academic paper has less workspace, hardness, and can be controlled with limited length.	The mechanism features a high magnetic volume and flexibility due to the spherical joints between the balls. This new class of robot offers a higher level of steering capability when compared to other magnetic robots. Combined with sensor-based feedback, the model is sufficiently accurate for closed-loop control.	When the robot approaches the axis, the angle a will be different from the calculated value because the chain will not be in a straight line. This is because the first magnet is fixed to the main axis, which resists the movement of the second ball.

Illustrative image	Article title	Compare to our work	Advantages
	A Magnetically-Actuated Coiling Soft Robot With Variable Stiffness[56]	The robot features a tongue-shaped structure with a sliding nitinol skeleton. It includes a visual feedback system utilizing a camera to monitor its position and orientation in real time. An image processing algorithm tracks the robot tip and adjusts the applied magnetic field to achieve the desired position. A nitinol wire integrated into the robot's structure enables adjustments in rigidity and shape, making it adaptable for various surgical tasks. Compared to our work, the robot in this paper has a smaller workspace.	The robot body is designed to undergo significant elastic deformation. A closed-loop control strategy enables it to grasp and release objects of different sizes. This is achieved by synchronising the sliding nitinol skeleton with the actuation of the magnetic field. The variable stiffness of this robot is advantageous for medical tools but can pose challenges during functional tasks.
	A Soft Robot with Three-Dimensional Shape Sensing and Contact Recognition Multi-Modal Sensing via Tunable Soft Optical Sensors[55]	A multimodal gripper with a soft optical sensor for precise tip tracking and contact detection is integrated into this robotic platform. It also features a multi-directional folding module with 3D shape recognition capabilities. Compared to our work, the robot in this paper is not suitable for confined spaces smaller than 20mm and cannot enter the bronchus.	The robot's body is designed for significant elastic deformation. It uses a closed-loop control strategy to grasp and release objects of different sizes. This is achieved by synchronising the sliding nitinol skeleton with the actuation of the magnetic field. While the variable stiffness is beneficial for medical tools, it can also present challenges during functional tasks.

Illustrative image	Article title	Compare to our work	Advantages
	A Fluidic Actuated Soft Robot for Improving Bronchoscopic Biopsy[58]	It is a flexible robot with a diameter of 3.5 mm and sufficient integrated degrees of freedom for tip control, tip stabilisation and needle deployment for tissue biopsy during bronchoscopy procedures. The robot can navigate through the pulmonary branches to the target lesion and anchor in an anatomical channel using soft actuators integrated into its continuous body. After anchoring, a needle can be deployed from the robot tip using an origami-inspired soft actuator to puncture the targeted lesion and perform a biopsy. Compared to our magnetically driven robot, the robot in this paper, which uses air actuation, has lower precision but greater driving force.	With a diameter of 3.5 mm, the robot can reach deep into the lungs. Compared to commercial bronchoscopy systems, it offers greater flexibility, safer tissue interactions, and a needle that punctures from the tip. These advantages are made possible by the robot's capability to actively increase stiffness by a factor of five.
	Independently Actuated Soft Magnetic Manipulators for Bimanual Operations in Confined Anatomical Cavities[57]	The robot is a modular monolithic double-helix soft magnetic manipulator design that promotes bending in the desired plane through mechanical constraint.The experimental setup also includes four Optitrack infrared cameras for 3D motion tracking. Compared to our work, the robot in this paper has a complex structure and high manufacturing costs.	Soft magnetic manipulators, actuated remotely, enable miniaturization while maintaining controllable degrees of freedom. Combining the scalability of monolithic magnetic manipulators with independent local actuation enhances endoscopic procedures, currently reliant on bulky, rigid tools, providing significant benefits for both patients and surgeons.

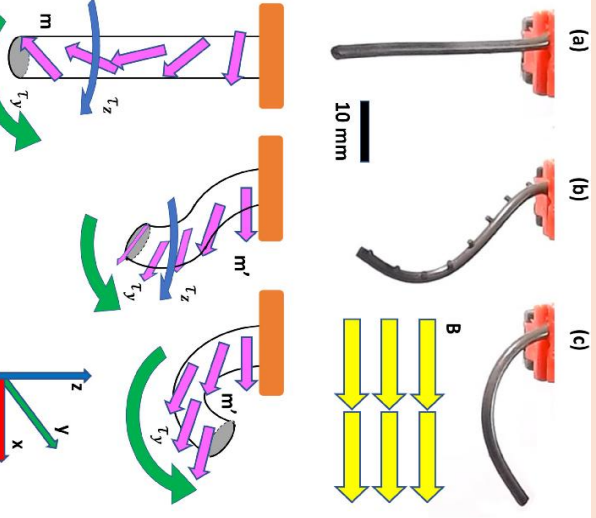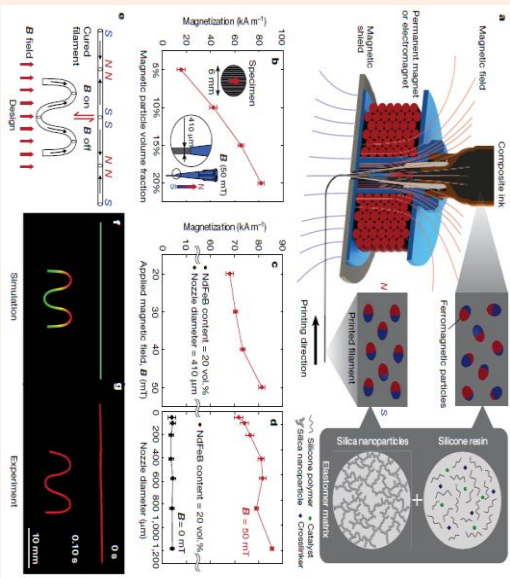| Illustrative image	Article title	Compare to our work	Advantages	Disadvantages
	Magnetic Soft Continuum Robots with Braided Reinforcement[10]	The Magnetic Continuum Robot (MCR) is made up of a chain of five rigid links, each 10 mm in length, connected by spring-loaded rotary joints with three degrees of freedom. Shaped like a braid, the system operates at a frequency of 2 Hz, allowing it to navigate 50 mm in 25 seconds. Compared to our robot, this paper reinforces the robot's body, but the 10mm length imposes limitations, as it cannot provide the same workspace as ours.	The braided design permits higher bend angles, enabling effective low-contact navigation through complex and tortuous areas.	Spatial navigation errors are attributed to the inaccurate positioning of the MCR origin, impacting the joint angle network and consequently the required actuation fields.
	Personalized magnetic tentacles for targeted photothermal cancer therapy in peripheral lungs[59]	This approach uses a 2.4mm diameter soft magnetic catheter. The catheter is deployed from the tip of a standard bronchoscope to access the peripheral regions of the lung. Integrated shape-sensing allows for supervised autonomous control, ensuring precise navigation within the subsegmental bronchi. Additionally, an integrated Laser Fibre facilitates treatment by delivering localised energy. Compared to our robot, this robot increases costs with its use of two manipulators and also increases the complexity of the algorithms.	The robot achieves an average navigation depth improvement of 37% with reduced tissue displacement compared to a standard semi-rigid catheter. Additionally, it demonstrates navigation depth repeatability within less than 1 mm across all tests. This represents a novel targeted therapeutic approach for the minimally invasive treatment of lung cancer.	While it minimally affects navigation performance, moving external permanent magnets can pose safety risks. Ghost experiments indicate that robots might enter unintended areas. In clinical settings, open-loop control can lead to undesired behavior during navigation or interactions with lung tissue due to errors in sensor readings and initial localization.

Illustrative image	Article title	Compare to our work	Advantages
	Dual-Arm Control for Enhanced Magnetic Manipulation[41] Patient-specific magnetic catheters for atraumatic autonomous endoscopy	Using a two-armed collaborative robot with permanent magnets at the tips, Giovanni et al. developed an innovative magnetic actuation method [40]. The core principle is that the strength of the magnetic field is a function of the distance from the magnet. By adjusting the position and orientation of the magnet, the strength and direction of the magnetic field can be controlled at specific locations. The robot arms, with their 8 degrees of freedom (DOFs), demonstrated effective manipulation of all 8 DOFs. Experiments showed that the average cross-activation error for unwanted DOFs was 2%-10%. Compared to our robot, the robot in this paper, with its use of two manipulators, increases both cost and the complexity of control algorithms.	The advantage of this manipulation technique lies in its ability to minimize costs and energy consumption while offering a larger target workspace compared to coil-based counterparts.
	Patient-specific magnetic catheters for atraumatic autonomous endoscopy [60]	Giovanni et al. designed a soft magnetic catheter consisting of three segments, with a length of 80 mm and a diameter of 2 mm, capable of navigating human anatomy using a permanent magnet guide. The segments, made of silicone and magnetic particles, are magnetized at different angles relative to the magnetic field. Figure 6 shows that varying magnetization methods allow the path to be programmed for navigation in confined environments. Two permanent magnets provide the necessary magnetic field as the two robot arms move to achieve the desired positioning. Compared to our robot design, this paper uses a method tailored for each custom robot to achieve better path adaptation, but it lacks universality, which increases costs.	The primary advancement is that the segmented design allows the catheter to be preprogrammed, increasing its ability to navigate various pathways, particularly in minimally invasive surgery (MIS). Additionally, the use of preoperative imaging enhances the accuracy and safety of the procedure.

Disadvantages	Illustrative image	Article title
Compared to a single robotic arm, dual-arm robots are more expensive and more difficult to control and coordinate.		A magnetically controlled soft microrobot steering a guidewire in a three-dimensional phantom vascular network[61]
Their versatility is relatively poor, as they can only navigate specific paths.		Ferromagnetic soft continuum robots[16]

Compare to our work	Advantages	Disadvantages	Illustrative image
Sungwoong et al. designed a magnetically controlled soft robot for steering a guidewire. The electromagnetic steering system, as shown, uses 8 electromagnets to create a uniform 3-dimensional magnetic field at the center of the coils. A camera provides a view of the microrobot's deformation. By adjusting the current in each coil, the direction and strength of the magnetic field can be varied. A master-slave system enables precise rectilinear motion, pulling the microrobot forward accurately with guidewire driving parts, catheter driving parts, and telescopic parts. An X-ray monitoring unit allows visualization of the robot inside the body, while a human-level interface provides feedback for monitoring the microrobot system. Compared to our method of controlling the robot with movable magnets, this paper uses several fixed electromagnetic coils, which limits its range of use and increases costs.	They can produce a uniform magnetic field and offer high control precision.	They are restricted to performing surgeries on small animals or within small organs.	
The authors [16] introduced a ferromagnetic soft robot with a diameter of 0.6 mm, incorporating an optical fiber for omnidirectional steering capabilities. The robot's surface is covered with hydrogel to reduce friction. The primary aim is to address conditions such as aneurysms, occlusions, stenosis, arteriovenous malformations, bronchitis, and arrhythmias, which are challenging to reach with minimal trauma. The soft robot's main body is made of polydimethylsiloxane (PDMS), chosen for its excellent biocompatibility, reducing the risk of bio-rejection. Neodymium-iron-boron (NdFeB) is used due to its ability to retain high remnant magnetization against external fields because of its high coercivity. Unlike soft magnetic materials like iron, which lose magnetization once the external field is removed, NdFeB maintains its magnetic properties, making it a common choice despite its toxicity. The hydrogel coating not only reduces friction but also mitigates the toxicity issue. In the mathematical modeling, the actuation tip is treated as a cantilever, simplifying the model by ignoring changes in the angle when the robot deflects. Compared to our work, the mathematical modeling in this paper overlooks the impact of the magnetic field and angle changes caused by robot deformation, which causes the modeling to fail under significant deformation.	They have low friction and a small radius, making them ideal for navigating finer blood vessels, and they are suitable for 3D printing.	They are only applicable for use in the brain and spherical organs.	

Article title	Compare to our work	Advantages	Disadvantages
Intelligent magnetic manipulation for gastrointestinal ultrasound[63] Millimeter-scale soft continuum robots for large-angle and high-precision manipulation by hybrid actuation	In this work, Joseph et al. propose a new magnetic capsule for minimally invasive surgery (MIS). This study demonstrated the potential for closed-loop magnetic control using digitized microanatomy (µUS) as feedback in both phantom and in vivo tests within a porcine model. Compared to our work, the paper integrates sensors into the design, but the resulting volume is too large to be used within bronchial branches.	The location accuracy of 1.0 ± 0.9 mm is crucial for ensuring robustness in complex environments, which enhances its application through closed-loop magnetic control.	The disadvantage of this capsule is its size measuring 21 mm in diameter and 39 mm in length that can not be used in smaller lumen.
Millimeter-scale soft continuum robots for large-angle and high-precision manipulation by hybrid actuation[62]	The robot is designed for applications in brain vessels, neck vessels, bronchus, and cardiac vessels. It contains iron particles and an antagonistic wire within its hollow skeleton, enabling navigation through vascular environments using magnetic fields and tendons. The soft robot is fabricated through 3D printing, coating, and axial magnetization. Its materials include silicone rubber (Ecoflex) and microiron particles in a constant mass ratio. Compared to our work, the paper employs a hybrid actuation approach, which compensates for the weakness of low force in pure magnetic actuation; however, the manufacturing process is complex and the costs are higher.	The primary advantage of this robot is its large inner lumen of 2.4 mm, allowing the use of various surgical tools during operations. Additionally, it can achieve a bending angle of up to 100°, improving its ability to navigate through twisted vessels. The magnetic actuation provides excellent precision, with static positioning accuracy of approximately 2 µm and dynamic tracking with an RMSE of around 10 µm. However, the hybrid actuation system increases both the complexity and cost of the overall setup.	Hybrid control is challenging, and the cost is high.

Illustrative image	Article title	Compare to our work	Advantages
	Braided Reinforcement magnetic soft robot[10]	This paper, created by Peter et al, present a high aspect ratio soft magnetic catheter with 2 mm diameter and 50 mm in length. They prove that it can navigating up to a 180°bend. They finished a contrast of undeformed, compound bending and twisting of an unreinforced, and pure bending of a braid reinfoced robot with the 20mT applied magnetic field. Compared to our work, the method proposed in the paper reduces axial rotation, but it results in a reduced robot workspace.	Compared to other MCR, this robot can only bending without twisting because of 1mm diameter nylon braid is inserted inside of it.
	Printing ferromagnetic domains for untethered fast-transforming soft materials[64]	Yoonho et al design a 3D printing The magnetic particles were pre-magnetized and are reoriented by applied magnetic field produced by a electromagnetic coil or a permanent magnet. According to the test the volume ratio of NdFeB particles in the ink positive correlation with magnetization. There also a design of MCR that curved like letter " M" when applying a magnetic field and the experiment almost same to the simulation. They also present some 2D and 3D structures with designed ferromagnetic domains and the results are similar to the design. Compared to our work, the paper proposed a method for manufacturing magnetic soft robots using 3D printing, which excels in customization capabilities; however, it requires the use of very high-intensity magnetic fields for control.	This kind of method enable lots of possibility of MCR and enable the fast manufacturing of it

Disadvantages	Illustrative image	Article title
The drawback is obvious that the workspace is too small to allow operation.		Modeling and validation of the three-dimensional deflection of an MRI-compatible magnetically actuated steerable catheter[66]
They require a high magnetic field for operation.		Magnetic continuum device with variable stiffness[65]

Compare to our work	Advantages
In 2016, Taoming et al. proposed a catheter actuated by the magnetic field generated by a magnetic resonance imaging (MRI) scanner. The catheter prototype used in experimental validation includes two current-carrying coil sets: a proximal coil set and a distal coil set. Each set comprises one 130-turn axial coil and two 30-turn side coils. The axial coil firmly grips the two side coils, creating an X-shaped cross directions. This configuration aligns the net magnetization vectors in the desired orthogonal between them. The coils, constructed by Adapt Industries, LLC (Salisbury, MD, USA), are made from thick insulated 38-gauge electromagnetic wires with enameled copper. Compared to our work, the method proposed in the paper for controlling electromagnetic coils using an external magnetic field is prone to generating heat.	They are suitable for generating strong electromagnetic forces and have robust driving capabilities.
This paper introduces a variable stiffness catheter utilizing a low melting point alloy (LMPA), a feature not found in other designs. It presents an innovative closed-loop temperature control scheme with a central working channel. During procedures like cardiac ablation and gastrointestinal surgery, the working channel can accommodate a functional tip or introduce a tool. A closed-loop temperature management system ensures overheating is prevented, thus avoiding cell damage. These functionalities are integrated while maintaining a 2.33 mm external diameter, addressing two major drawbacks of the previous design. Figure 36 illustrates the variable stiffness continuous device with a central working channel that can be used for cable actuation (e.g., a cable through the channel to operate a gripper) or active cooling (e.g., irrigation fluid passing through the channel), depending on the surgical scenario. The prototype includes components such as a Cerrolow 117 inner flexible tube, three heaters, a magnet, and a silicone tube encasing the entire assembly, with an external diameter of 2.5 mm. The three heaters, made of enameled copper wire coils surrounding inner tubes, form three independent variable stiffness segments. Plastic spacers separate the flexible inner tube from the continuum device's tubular structure, which is coaxial to it. Compared to our work, the paper proposes a catheter with variable stiffness, but its complex structure increases manufacturing difficulty and costs.	Compared to other magnetic continuum devices, the variable stiffness (VS) device significantly enhances manipulability. Its small diameter and central working channel make it suitable for various minimally invasive treatments in organs with narrow access pathways, such as the gastrointestinal system and heart chambers. In cardiac arrhythmia ablation, the VS magnetic continuum device allows for multiple bending radii and reduces the number of magnets needed from three to one compared to conventional magnetic catheters. The device can be rigidified for increased stability or selectively softened to allow deflection under a magnetic field.

Disadvantages	Illustrative image
Electromagnetic coils limit the size of the catheter and generate heat.	
The structure is complex, and the manufacturing difficulty is high.	

B. Appendix

COMSOL simulation results used to measure the angle and working distance:
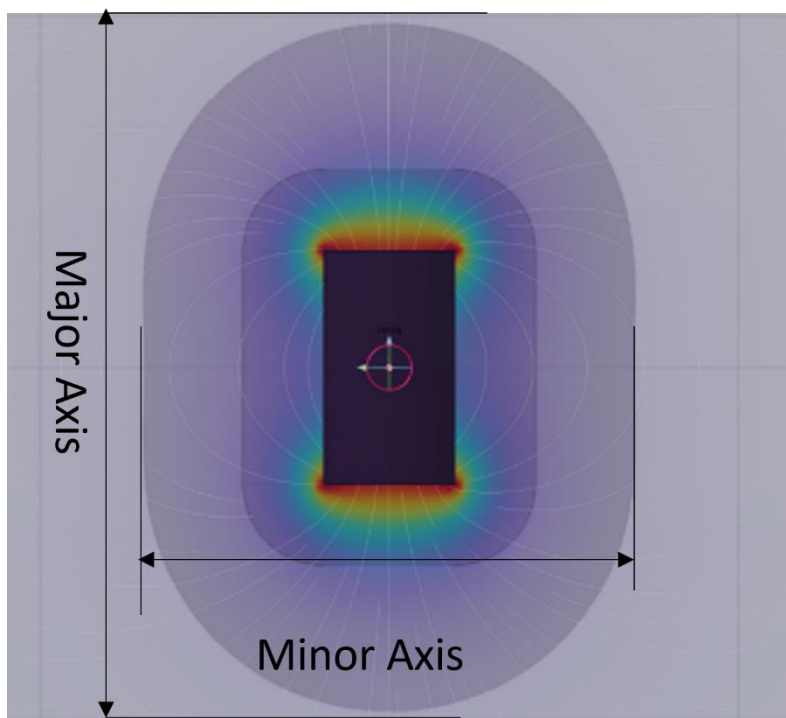
Figure 26 Example of showing Minor Axis and Major Axis

Figure 26 elucidates the major and minor axes. Employing the methodology mentioned in the COMSOL simulation, we can generate images like following image(Table 2,Table 3,Table 4,Table 5,Table 6). Subsequently, using ImageJ software, we measured α, β, γ, δ, ε, ζ from Figure 13(b), which then led to the creation of Figure 23.

Table 2 :R-radius of magnet, H-height of magnet

1)R5cm-H40cm-34mT	2)R5cm-H40cm-20mT	3) R5cm-H36cm-34mT
4) R5cm-H36cm-20mT	5) R5cm-H32cm-34mT	6) R5cm-H32cm-20mT

7) R5cm-H28cm-34mT	8) R5cm-H28cm-20mT	9) R5cm-H24cm-34mT
10) R5cm-H24cm-20mT	11) R5cm-H20cm-34mT	12) R5cm-H20cm-20mT
13) R5cm-H16cm-34mT	14) R5cm-H16cm-20mT	15) R5cm-H12cm-34mT
16) R5cm-H12cm-20mT	17) R5cm-H8cm-34mT	18) R5cm-H8cm-20mT
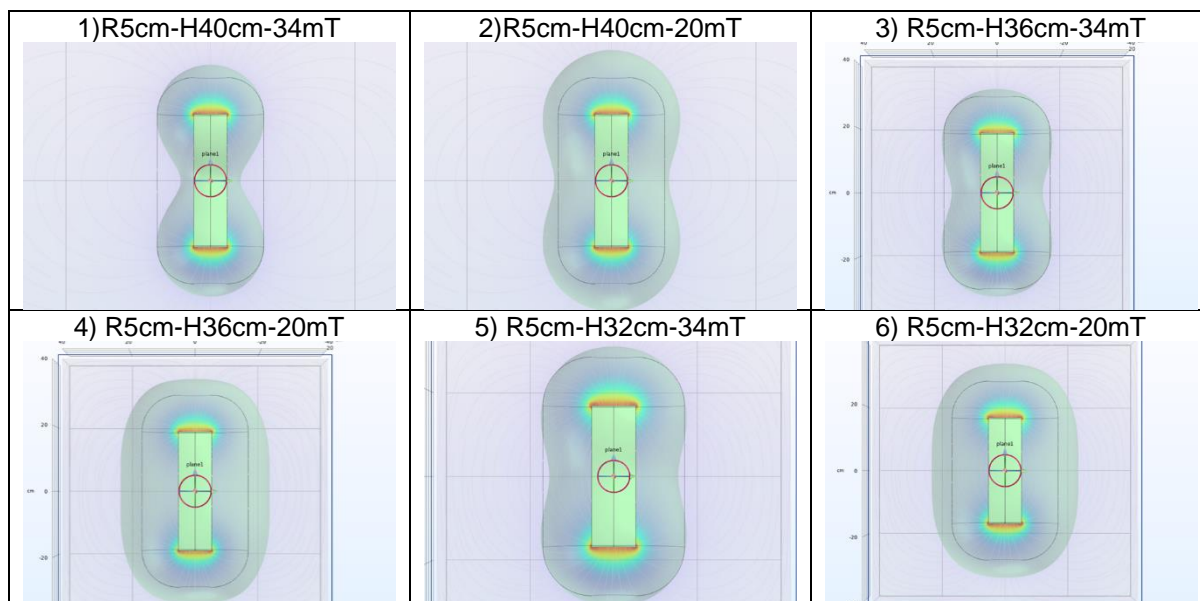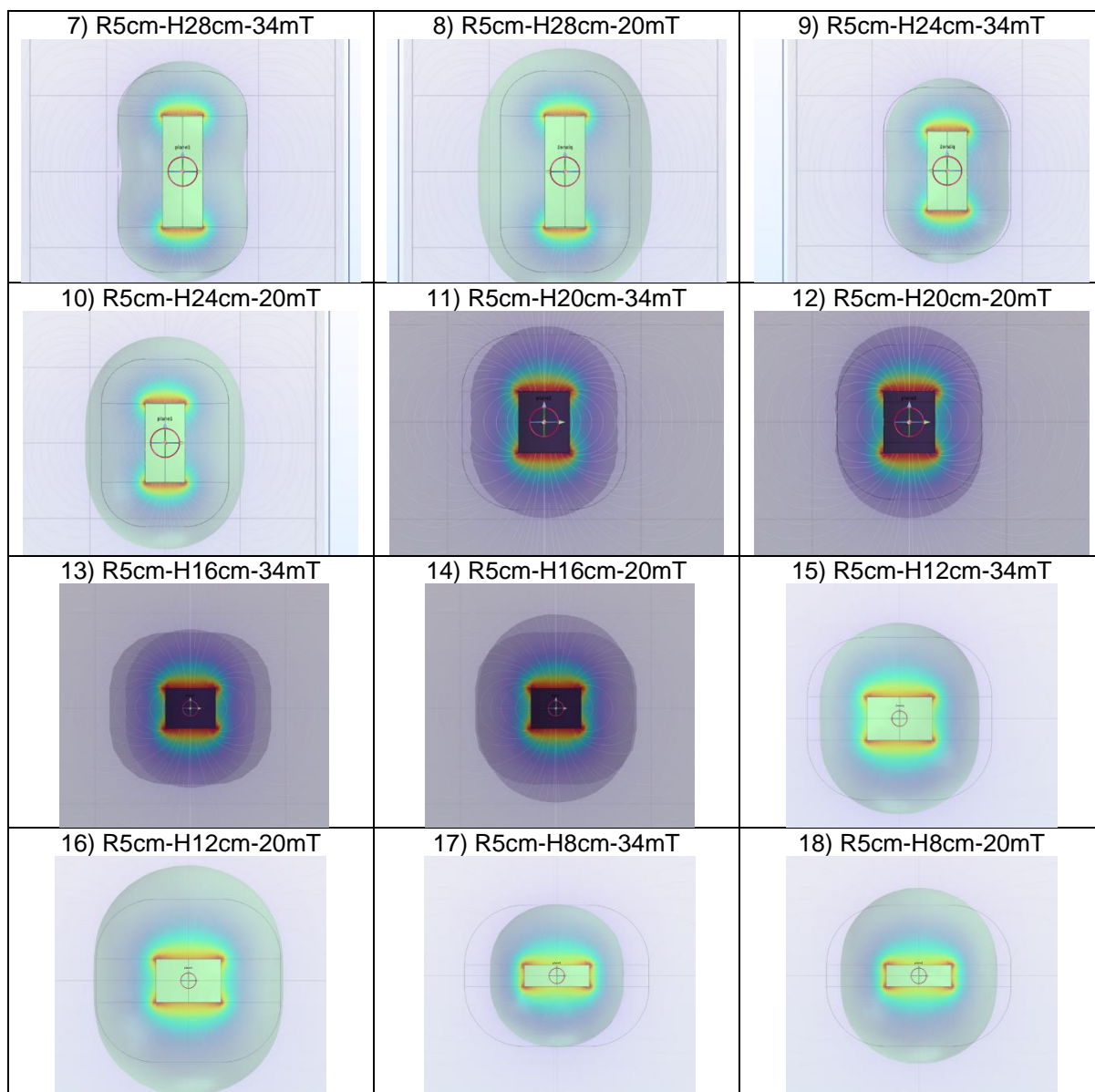
Table 3:R-radius of magnet, H-height of magnet

1) R6cm-H40cm-34mT	2) R6cm-H40cm-20mT	3) R6cm-H36cm-34mT

4) R6cm-H36cm-20mT	5) R6cm-H32cm-34mT	6) R6cm-H32cm-20mT
7) R6cm-H28cm-34mT	8) R6cm-H28cm-20mT	9) R6cm-H24cm-34mT
10) R6cm-H24cm-20mT	11) R6cm-H20cm-34mT	12) R6cm-H20cm-20mT
13) R6cm-H16cm-34mT	14) R6cm-H16cm-20mT	15) R6cm-H12cm-34mT
16) R6cm-H12cm-20mT	17) R6cm-H8cm-34mT	18) R6cm-H8cm-20mT
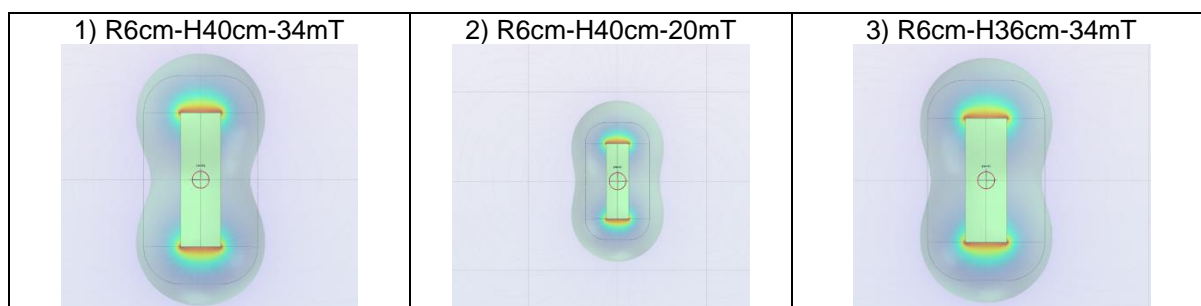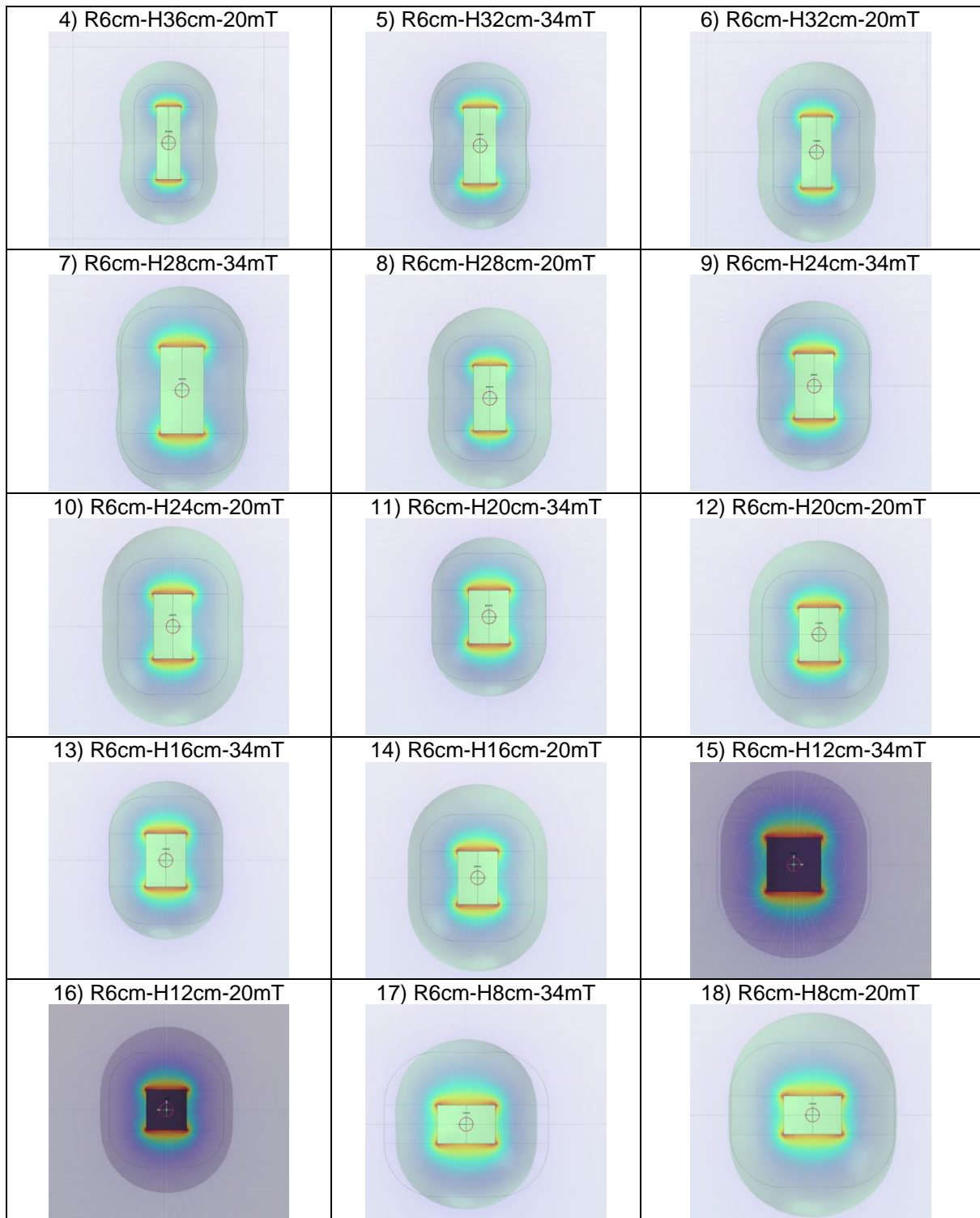
Table 4:R-radius of magnet, H-height of magnet

1) R7cm-H40cm-34mT	2) R7cm-H40cm-20mT	3) R7cm-H36cm-34mT
4) R7cm-H36cm-20mT	5) R7cm-H32cm-34mT	6) R7cm-H32cm-20mT
7) R7cm-H28cm-34mT	8) R7cm-H28cm-20mT	9) R7cm-H24cm-34mT
10) R7cm-H24cm-20mT	11) R7cm-H20cm-34mT	12) R7cm-H20cm-34mT
13) R7cm-H16cm-34mT	14) R7cm-H16cm-20mT	15) R7cm-H12cm-34mT
16) R7cm-H12cm-20mT	17) R7cm-H8cm-34mT	18) R7cm-H8cm-20mT

Table 5:R-radius of magnet, H-height of magnet

16) R8cm-H12cm-20mT	17) R8cm-H8cm-34mT	18) R8cm-H8cm-20mT
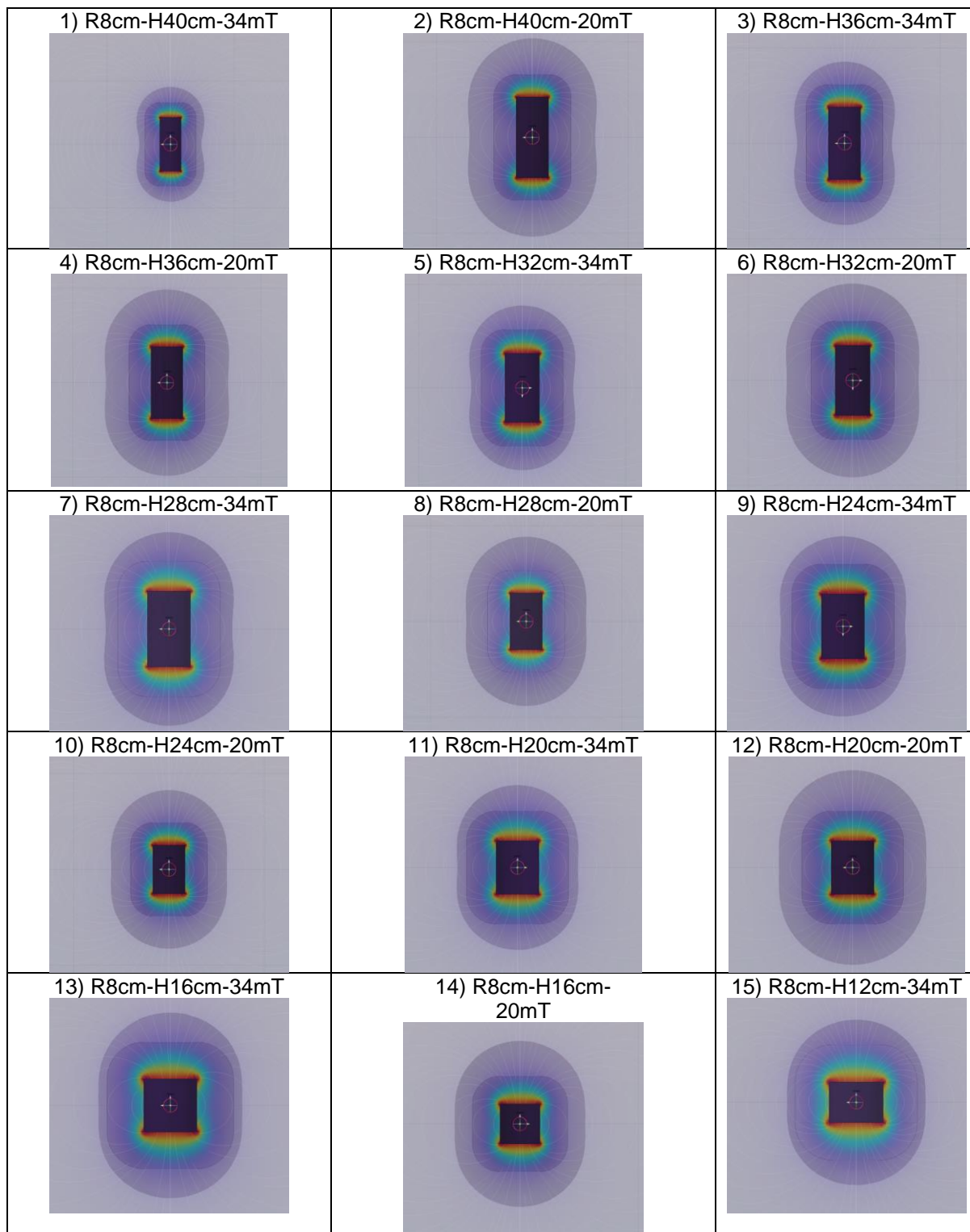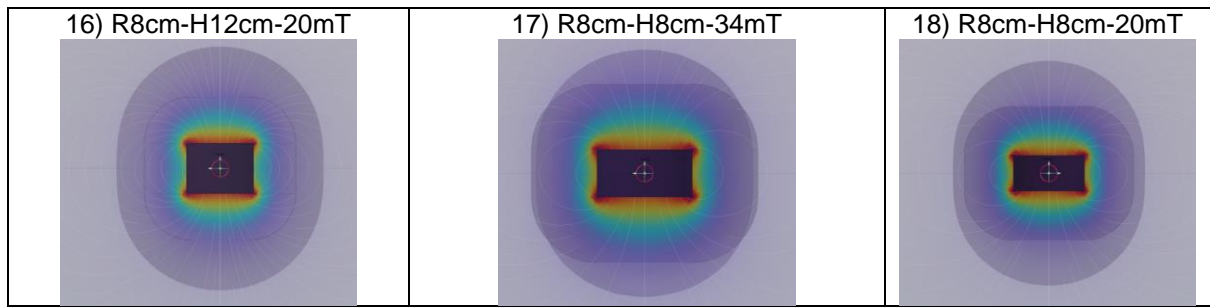
Table 6:R-radius of magnet, H-height of magnet

1) R9cm-H40cm-34mT	2) R9cm-H40cm-20mT	3) R9cm-H36cm-34mT
4) R9cm-H36cm-20mT	5) R9cm-H32cm-34mT	6) R9cm-H32cm-20mT
7) R9cm-H28cm-34mT	8) R9cm-H28cm-20mT	9) R9cm-H24cm-34mT
10) R9cm-H24cm-20mT	11) R9cm-H20cm-34mT	12) R9cm-H20cm-20mT
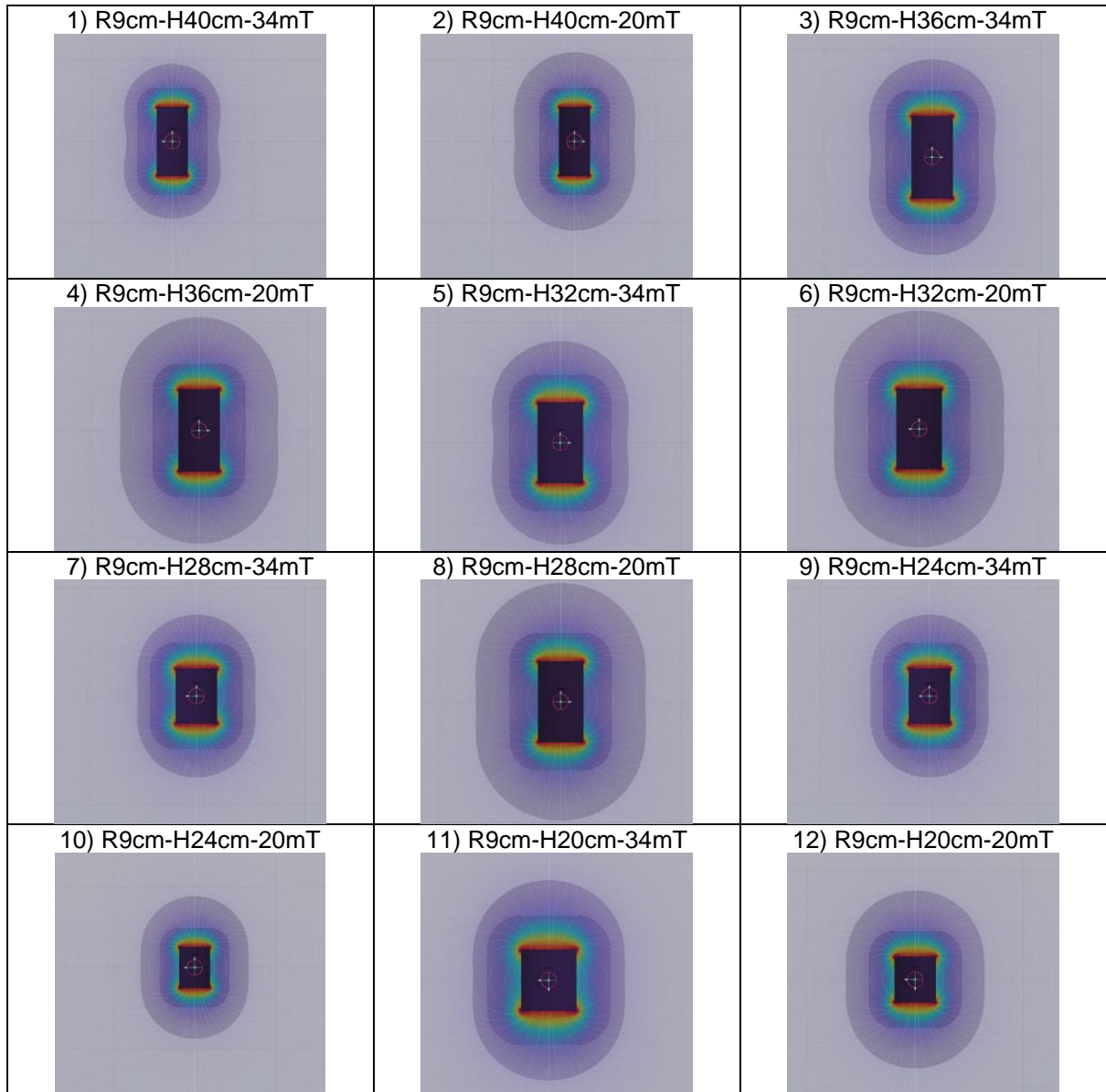
C. Appendix

Table 7 Experimental measurements of calibration error

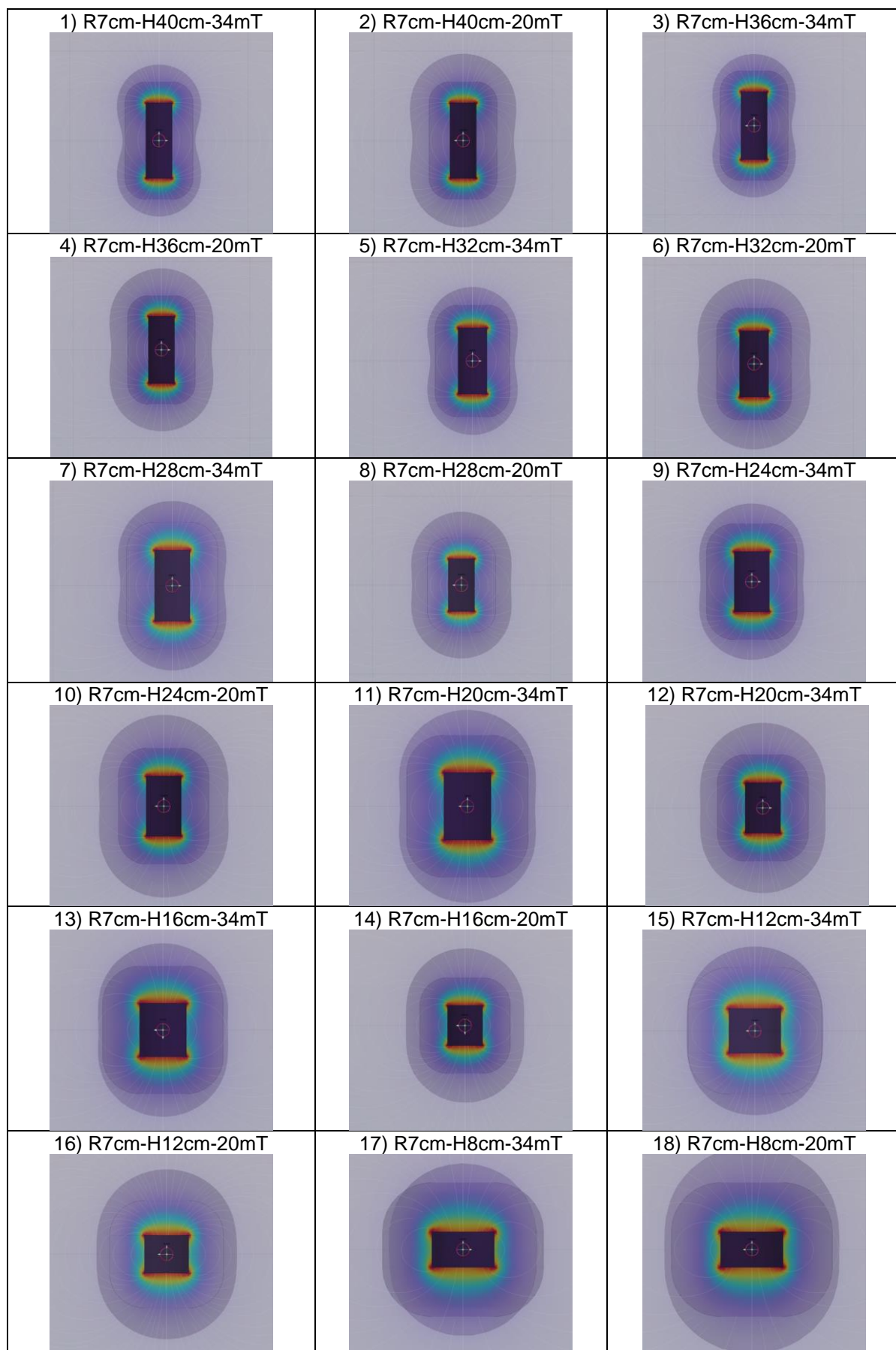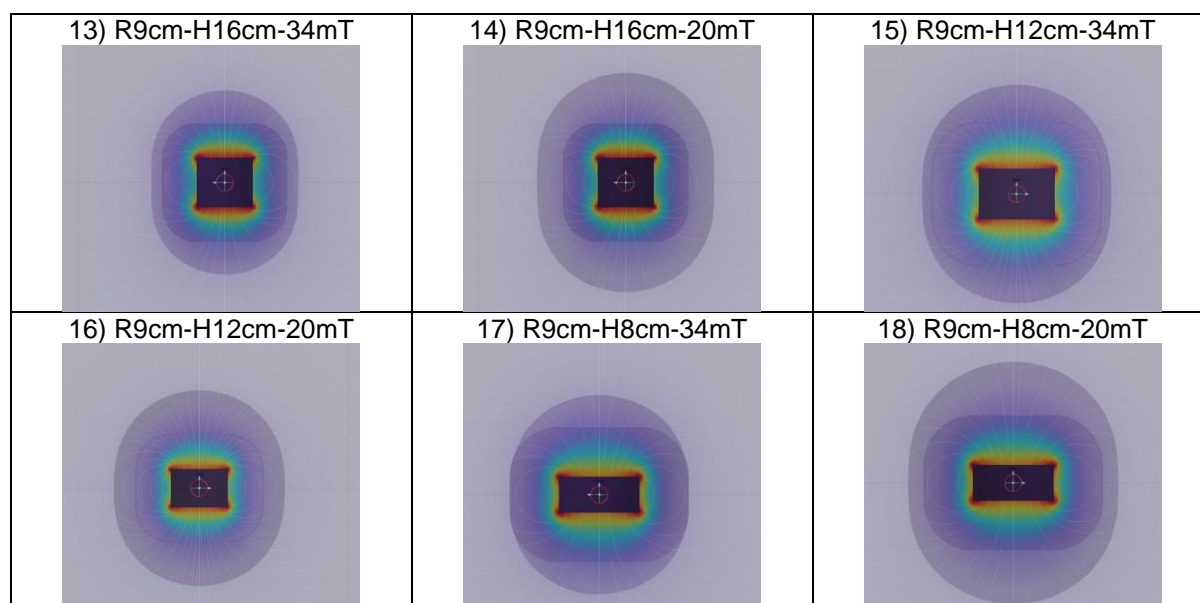|	Trail 1	Trail 2	Trail 3	Trail 4	Trail 5	Trail 6	Mean	Standard deviation
Distance/mm	5.889	6.091	6.064	5.947	5.978	6.911	6.038	0.0071

Table 8 Experimental results of manual measurement of distance and angle

	Trail 1	Trail 2	Trail 3	Trail 4	Trail 5	Trial 6	Mean	Standard deviation
Distance/mm	60.408	60.432	61.099	60.387	60.872	60.861	60.676	0.279
Angle/°	10.2	10.3	9.8	9.9	10.1	10.0	10.05	0.1708

References

[1]   A. Darzi and Y. Munz, "The impact of minimally invasive surgical techniques," *Annu. Rev. Med.,* vol. 55, pp. 223-237, 2004.

[2]   Z. Yang and L. Zhang, "Magnetic actuation systems for miniature robots: A review," *Advanced Intelligent Systems,* vol. 2, no. 9, p. 2000082, 2020.

[3]   J. Edelmann, A. J. Petruska, and B. J. Nelson, "Magnetic control of continuum devices," *The International Journal of Robotics Research,* vol. 36, no. 1, pp. 68-85, 2017, doi: 10.1177/0278364916683443.

[4]   S. Jeon *et al.*, "Improving guidewire-mediated steerability of a magnetically actuated flexible microrobot," *Micro and Nano Systems Letters,* vol. 6, no. 1, 2018, doi: 10.1186/s40486-018-0077-y.

[5]   T. Greigarn, N. L. Poirot, X. Xu, and M. C. Cavusoglu, "Jacobian-Based Task-Space Motion Planning for MRI-Actuated Continuum Robots," *IEEE Robot Autom Lett,* vol. 4, no. 1, pp. 145-152, Jan 2019, doi: 10.1109/LRA.2018.2881987.

[6]   G. Pittiglio, J. H. Chandler, M. Richter, V. K. Venkiteswaran, S. Misra, and P. Valdastri, "Dual-Arm Control for Enhanced Magnetic Manipulation," presented at the 2020 IEEE/RSJ International Conference on Intelligent Robots and Systems (IROS), 2020.

[7]   L. Wang, Y. Kim, C. F. Guo, and X. Zhao, "Hard-magnetic elastica," *Journal of the Mechanics and Physics of Solids,* vol. 142, 2020, doi: 10.1016/j.jmps.2020.104045.

[8]   P. Lloyd, Z. Koszowska, M. Di Lecce, O. Onaizah, J. H. Chandler, and P. Valdastri, "Feasibility of Fiber Reinforcement Within Magnetically Actuated Soft Continuum Robots," *Front Robot AI,* vol. 8, p. 715662, 2021, doi: 10.3389/frobt.2021.715662.

[9]   Y. Kim *et al.*, "Telerobotic neurovascular interventions with magnetic manipulation," *Science Robotics,* vol. 7, no. 65, p. eabg9907, 2022.

[10]   P. Lloyd, O. Onaizah, G. Pittiglio, D. K. Vithanage, J. H. Chandler, and P. Valdastri, "Magnetic Soft Continuum Robots With Braided Reinforcement," *IEEE Robotics and Automation Letters,* vol. 7, no. 4, pp. 9770-9777, 2022, doi: 10.1109/lra.2022.3191552.

[11]   G. Pittiglio *et al.*, "Patient-Specific Magnetic Catheters for Atraumatic Autonomous Endoscopy," *Soft Robot,* vol. 9, no. 6, pp. 1120-1133, Dec 2022, doi: 10.1089/soro.2021.0090.

[12]   D. Lin, W. Chen, K. He, N. Jiao, Z. Wang, and L. Liu, "Position and Orientation Control of Multisection Magnetic Soft Microcatheters," *IEEE/ASME Transactions on Mechatronics,* vol. 28, no. 2, pp. 907-918, 2023, doi: 10.1109/tmech.2022.3213934.

[13]   G. Pittiglio *et al.*, "Personalized magnetic tentacles for targeted photothermal cancer therapy in peripheral lungs," *Communications Engineering,* vol. 2, no. 1, 2023, doi: 10.1038/s44172-023-00098-9.

[14]   R. Dreyfus *et al.*, "Dexterous helical magnetic robot for improved endovascular access," *Science Robotics,* vol. 9, no. 87, p. eadh0298, 2024.

[15]   V. Lalande *et al.*, "In vivo demonstration of magnetic guidewire steerability in a MRI system with additional gradient coils," *Medical physics,* vol. 42, no. 2, pp. 969-976, 2015.

[16]   Y. Kim, G. A. Parada, S. Liu, and X. Zhao, "Ferromagnetic soft continuum robots," *Science Robotics,* vol. 4, no. 33, p. eaax7329, 2019.

[17]   K. Wadowska, I. Bil-Lula, Ł. Trembecki, and M. Śliwińska-Mosson, "Genetic markers in lung cancer diagnosis: a review," *International journal of molecular sciences,* vol. 21, no. 13, p. 4569, 2020.

[18]   L. G. Collins, C. Haines, R. Perkel, and R. E. Enck, "Lung cancer: diagnosis and management," *American family physician,* vol. 75, no. 1, pp. 56-63, 2007.

[19]   M. P. Rivera, F. Detterbeck, and A. C. Mehta, "Diagnosis of lung cancer: the guidelines," *Chest,* vol. 123, no. 1, pp. 129S-136S, 2003.

[20]   A. C. Arroliga and R. A. Matthay, "The role of bronchoscopy in lung cancer," *Clinics in chest medicine,* vol. 14, no. 1, pp. 87-98, 1993.

[21]   S. J. Mentzer, "Mediastinoscopy, thoracoscopy, and video-assisted thoracic surgery in the diagnosis and staging of lung cancer," *Hematology/oncology clinics of North America,* vol. 11, no. 3, pp. 435-447, 1997.

[22]   V. Vitiello, S.-L. Lee, T. P. Cundy, and G.-Z. Yang, "Emerging robotic platforms for minimally invasive surgery," *IEEE reviews in biomedical engineering,* vol. 6, pp. 111-126, 2012.

[23]   B. Jaffray, "Minimally invasive surgery," *Archives of disease in childhood,* vol. 90, no. 5, pp. 537-542, 2005.

[24]   W. W. G. Ee, W. L. J. Lau, W. Yeo, Y. Von Bing, and W. M. Yue, "Does minimally invasive surgery have a lower risk of surgical site infections compared with open spinal surgery?," *Clinical Orthopaedics and Related Research®,* vol. 472, pp. 1718-1724, 2014.

[25]   H.-J. Tan, J. S. Wolf, Z. Ye, K. S. Hafez, and D. C. Miller, "Population level assessment of hospital based outcomes following laparoscopic versus open partial nephrectomy during the adoption of minimally invasive surgery," *The Journal of urology,* vol. 191, no. 5, pp. 1231-1237, 2014.

[26]   K. Bostanci *et al.*, "Quality of life of patients who have undergone the minimally invasive repair of pectus carinatum," *European Journal of Cardio-Thoracic Surgery,* vol. 43, no. 1, pp. 122-126, 2013.

[27]   N. Simaan, R. M. Yasin, and L. Wang, "Medical technologies and challenges of robot-assisted minimally invasive intervention and diagnostics," *Annual Review of Control, Robotics, and Autonomous Systems,* vol. 1, pp. 465-490, 2018.

[28]   J. Ferlay *et al.*, "Cancer statistics for the year 2020: An overview," *International journal of cancer,* vol. 149, no. 4, pp. 778-789, 2021.

[29]   R. Nooreldeen and H. Bach, "Current and future development in lung cancer diagnosis," *International journal of molecular sciences,* vol. 22, no. 16, p. 8661, 2021.

[30]   M. Andolfi, R. Potenza, R. Capozzi, V. Liparulo, F. Puma, and K. Yasufuku, "The role of bronchoscopy in the diagnosis of early lung cancer: a review," *Journal of thoracic disease,* vol. 8, no. 11, p. 3329, 2016.

[31]   M. McCandless, A. Perry, N. DiFilippo, A. Carroll, E. Billatos, and S. Russo, "A soft robot for peripheral lung cancer diagnosis and therapy," *Soft Robotics,* vol. 9, no. 4, pp. 754-766, 2022.

[32]   S. D. Murgu, "Robotic assisted-bronchoscopy: technical tips and lessons learned from the initial experience with sampling peripheral lung lesions," *BMC pulmonary medicine,* vol. 19, pp. 1-8, 2019.

[33]   J. Burgner-Kahrs, D. C. Rucker, and H. Choset, "Continuum robots for medical applications: A survey," *IEEE Transactions on Robotics,* vol. 31, no. 6, pp. 1261-1280, 2015.

[34]   G. Iddan, G. Meron, A. Glukhovsky, and P. Swain, "Wireless capsule endoscopy," *Nature,* vol. 405, no. 6785, pp. 417-417, 2000.

[35]   S. Tognarelli, C. Quaglia, P. Valdastri, E. Susilo, A. Menciassi, and P. Dario, "Innovative stopping mechanism for esophageal wireless capsular endoscopy," *Procedia Chemistry,* vol. 1, no. 1, pp. 485-488, 2009.

[36]   K. Ikuta, Y. Matsuda, D. Yajima, and Y. Ota, "Pressure pulse drive: A control method for the precise bending of hydraulic active catheters," *IEEE/ASME Transactions on Mechatronics,* vol. 17, no. 5, pp. 876-883, 2011.

[37]   Y. Bailly, Y. Amirat, and G. Fried, "Modeling and control of a continuum style microrobot for endovascular surgery," *IEEE Transactions on Robotics,* vol. 27, no. 5, pp. 1024-1030, 2011.

[38]   S. Guo, T. Fukuda, K. Kosuge, F. Arai, K. Oguro, and M. Negoro, "Micro catheter system with active guide wire," in *Proceedings of 1995 IEEE International Conference on Robotics and Automation*, 1995, vol. 1: IEEE, pp. 79-84.

[39]   H. Su, G. Li, D. C. Rucker, R. J. Webster III, and G. S. Fischer, "A concentric tube continuum robot with piezoelectric actuation for MRI-guided closed-loop targeting," *Annals of biomedical engineering,* vol. 44, pp. 2863-2873, 2016.

[40]   H. Su *et al.*, "A MRI-guided concentric tube continuum robot with piezoelectric actuation: A feasibility study," in *2012 IEEE International Conference on Robotics and Automation*, 2012: IEEE, pp. 1939-1945.

[41]   G. Pittiglio, J. H. Chandler, M. Richter, V. K. Venkiteswaran, S. Misra, and P. Valdastri, "Dual-arm control for enhanced magnetic manipulation," in *2020 IEEE/RSJ International Conference on Intelligent Robots and Systems (IROS)*, 2020: IEEE, pp. 7211-7218.

[42]   M. P. Kummer, J. J. Abbott, B. E. Kratochvil, R. Borer, A. Sengul, and B. J. Nelson, "OctoMag: An Electromagnetic System for 5-DOF Wireless Micromanipulation," *IEEE Transactions on Robotics,* vol. 26, no. 6, pp. 1006-1017, 2010, doi: 10.1109/tro.2010.2073030.

[43]   J. Sikorski, S. Mohanty, and S. Misra, "MILiMAC: Flexible Catheter With Miniaturized Electromagnets as a Small-Footprint System for Microrobotic Tasks," *IEEE Robotics and Automation Letters,* vol. 5, no. 4, pp. 5260-5267, 2020, doi: 10.1109/lra.2020.3004323.

[44]   S. L. Charreyron, B. Zeydan, and B. J. Nelson, "Shared control of a magnetic microcatheter for vitreoretinal targeted drug delivery," in *2017 IEEE international conference on robotics and automation (ICRA)*, 2017: IEEE, pp. 4843-4848.

[45]   R. Alsangur, S. Doğanay, I. Ates, A. Turgut, and L. Cetin, "3D Helmholtz coil system setup for thermal conductivity measurements of magnetic nanofluids," *Mechatronics,* vol. 94, p. 103019, 2023.

[46]   G. Ciuti, P. Valdastri, A. Menciassi, and P. Dario, "Robotic magnetic steering and locomotion of capsule endoscope for diagnostic and surgical endoluminal procedures," *Robotica,* vol. 28, no. 2, pp. 199-207, 2009, doi: 10.1017/s0263574709990361.

[47]   Z. Koszowska, G. Pittiglio, J. Chandler, M. Brockdorff, and P. Valdastri, "Mechanical Reinforcement Towards Fully Soft Magnetic Endoscopic Endonasal Surgical Manipulators," in *Hamlyn Symposium on Medical Robotics*, 2022, p. 73.

[48]   S. L. Charreyron, Q. Boehler, A. N. Danun, A. Mesot, M. Becker, and B. J. Nelson, "A magnetically navigated microcannula for subretinal injections," *IEEE transactions on biomedical engineering,* vol. 68, no. 1, pp. 119-129, 2020.

[49]   S. Yang, J. Kim, S. J. Choi, and K. W. Lee, "Determining average linear dimension and volume of korean lungs for lung phantom construction," *Health Physics,* vol. 120, no. 5, pp. 487-494, 2021.

[50]   "ImageJ software." https://imagej.net/ij/ (accessed July 1, 2024).

[51]   T. Zhang, L. Yang, X. Yang, R. Tan, H. Lu, and Y. Shen, "Millimeter-Scale Soft Continuum Robots for Large-Angle and High-Precision Manipulation by Hybrid Actuation," *Adv Intell Syst,* vol. 3, no. 2, p. 2000189, Feb 2021, doi: 10.1002/aisy.202000189.

[52]   M. McCandless, A. Perry, N. DiFilippo, A. Carroll, E. Billatos, and S. Russo, "A Soft Robot for Peripheral Lung Cancer Diagnosis and Therapy," *Soft Robot,* vol. 9, no. 4, pp. 754-766, Aug 2022, doi: 10.1089/soro.2020.0127.

[53]   G. Pittiglio, M. Mencattelli, and P. E. Dupont, "Closed-form kinematic model and workspace characterization for magnetic ball chain robots," in *2023 International Symposium on Medical Robotics (ISMR)*, 2023: IEEE, pp. 1-7.

[54]   G. Pittiglio *et al.*, "Closed loop static control of multi-magnet soft continuum robots," *IEEE Robotics and Automation Letters,* 2023.

[55]   M. McCandless, F. J. Wise, and S. Russo, "A soft robot with three dimensional shape sensing and contact recognition multi-modal sensing via tunable soft optical sensors," in *2023 IEEE International Conference on Robotics and Automation (ICRA)*, 2023: IEEE, pp. 573-580.

[56]   P. Lloyd *et al.*, "A magnetically-actuated coiling soft robot with variable stiffness," *IEEE Robotics and Automation Letters,* vol. 8, no. 6, pp. 3262-3269, 2023.

[57]   Z. Koszowska *et al.*, "Independently Actuated Soft Magnetic Manipulators for Bimanual Operations in Confined Anatomical Cavities," *Advanced Intelligent Systems,* vol. 6, no. 2, p. 2300062, 2024.

[58]   D. Van Lewen, T. Janke, H. Lee, R. Austin, E. Billatos, and S. Russo, "A Fluidic Actuated Soft Robot for Improving Bronchoscopic Biopsy."

[59]   G. Pittiglio *et al.*, "Personalized magnetic tentacles for targeted photothermal cancer therapy in peripheral lungs," *Communications Engineering,* vol. 2, no. 1, p. 50, 2023.

[60]   G. Pittiglio *et al.*, "Patient-specific magnetic catheters for atraumatic autonomous endoscopy," *Soft robotics,* vol. 9, no. 6, pp. 1120-1133, 2022.

[61]   S. Jeon *et al.*, "A magnetically controlled soft microrobot steering a guidewire in a three-dimensional phantom vascular network," *Soft robotics,* vol. 6, no. 1, pp. 54-68, 2019.

[62]   T. Zhang, L. Yang, X. Yang, R. Tan, H. Lu, and Y. Shen, "Millimeter‐scale soft continuum robots for large‐angle and high‐precision manipulation by hybrid actuation," *Advanced Intelligent Systems,* vol. 3, no. 2, p. 2000189, 2021.

[63]   J. C. Norton *et al.*, "Intelligent magnetic manipulation for gastrointestinal ultrasound," *Science robotics,* vol. 4, no. 31, p. eaav7725, 2019.

[64]   Y. Kim, H. Yuk, R. Zhao, S. A. Chester, and X. Zhao, "Printing ferromagnetic domains for untethered fast-transforming soft materials," *Nature,* vol. 558, no. 7709, pp. 274-279, 2018.

[65]   C. Chautems, A. Tonazzini, Q. Boehler, S. H. Jeong, D. Floreano, and B. J. Nelson, "Magnetic continuum device with variable stiffness for minimally invasive surgery," *Advanced Intelligent Systems,* vol. 2, no. 6, p. 1900086, 2020.

[66]   T. Liu, N. L. Poirot, D. Franson, N. Seiberlich, M. A. Griswold, and M. C. Çavuşoğlu, "Modeling and validation of the three-dimensional deflection of an MRI-compatible

magnetically actuated steerable catheter," *IEEE Transactions on Biomedical Engineering,* vol. 63, no. 10, pp. 2142-2154, 2015.